Origin of the Triassic Qilinchang Pb-Zn deposit in the western Yangtze block, SW China: Insights from in-situ trace elemental compositions of base metal sulphides

Abiola Oyebamiji[a,b], Ruizhong Hu[a,b,*], Chenghai Zhao[a], Tehseen Zafar[a]

[a] State Key Laboratory of Ore Deposit Geochemistry, Institute of Geochemistry, Chinese Academy of Sciences, Guiyang 550081, China
[b] College of Earth and Planetary Sciences, University of Chinese Academy of Sciences, Beijing 100049, China

ARTICLE INFO

ABSTRACT

The Qilinchang Pb-Zn deposit (ɕ 5Mt of sulphide ore at mean grades of 2.3–9.2% Pb and 2.7–22.5% Zn) is hosted in Early Carboniferous carbonate rocks and mainly controlled by NE-, NS-, and NW- trending structural belts between the Xiaojiang and Zhaotong-Qujing buried faults. Ore minerals are sphalerite, galena, pyrite, chalcopyrite, and marmatite, whereas gangue minerals are dolomite, calcite, and quartz. Three generations of pyrite are recognized; these include fine-grained anhedral pyrite (Py-I), medium-grained anhedral to subhedral hydrothermal pyrite (Py-II), and coarse-grained subhedral to euhedral hydrothermal pyrite (Py-III), while the sphalerite occurs in two forms as fine-grained intergrown with galena and associated with Py-I and Py-II.

Laser-ablation inductively coupled plasma mass spectrometry (LA-ICP-MS) analysis was performed to evaluate trace element compositions of pyrite and sphalerite from different generations of ores. Py-I has relatively higher concentrations of Mg, Mn, Co, Ni, and Tl. Py-II in Cu, As, Se, Mo, and Sb relative to pyrite of other generations. The contents of trace elements in Py-III are variable but significantly enriched in Ti, V, Bi, Ag, and Pb compared to Py-I and Py-II. This variation indicates that these elements occur as micro mineral inclusions of possible Ag-Pb-bearing phases. Sphalerite of stage I has higher concentrations of Mn, Fe, Co, Ni, Cu, Ga, Ge, As, Ag, Cd, In, Sb, Hg, and Pb than stage II. These elements are homogeneously distributed in all samples analyzed. The incorporation of these elements is primarily through simple substitution mechanisms (e.g., $2Zn^{2+} \leftrightarrow Cu^{+} + In^{3+}$) as indicated from binary plots. Principal component analyses (PCA) applied to LA-ICP-MS dataset for pyrite reveal two main clusters; Py-I enriched in Ni, Co and As, Py-II and Py-III high in with V, Mn, Cu, Zn, Se, Mo, Ag, Sb, Au, and Bi. Likewise, the PCA also confirms two clusters of elements for sphalerite; Ge, Cu, As, Sb, Ag, Fe, and Cd corresponding to Sph-I and In, Sn, and Ga corresponding to Sph-II.

Py-I has higher Co/Ni ratio ranging from 0.04 to 1.6 compared to Py-II and Py-III having Co/Ni ratios from 0 to 0.706 and 0 0.696, respectively. We report that the pyrites from the Qilinchang deposit have Co/Ni ratios slightly lower than typical Mississippi Valley-Type (MVT) deposits (0.2–7.2) and different from iron oxide copper-gold (IOCG) and porphyry Cu deposits. Considering these geochemical signatures, it can be suggested that the Qilinchang deposit was not related to magmatic activities. We thus propose that the ore-forming fluids responsible for the formation of the deposit were generated from a low-temperature environment, similar to typical MVT deposits.

1. Introduction

The base metal deposits in the Sichuan-Yunnan-Guizhou (SYG) metallogenic province contain over 400 known Pb-Zn deposits with total Pb + Zn metal reserves of approximately 26 million tons (Liu and Lin, 1999; Huang et al., 2004; Han et al., 2007; Zaw et al., 2007; Zhou et al., 2013; Zhang et al., 2015). Tectonically, this SYG metallogenic domain is westbound on the Yangtze Platform, southwestern part of China. Previous researches on the Qilinchang Pb-Zn deposit (Han et al., 2007) have categorized it to be large in scale, consistent, and highly mineable ore quality enriched in Ge, Pb, and Zn. These studies were mostly concerned with the deposit geology, isotope and element geochemistry (Han et al., 2004, 2007, 2012; Huang et al., 2004; Li et al., 2004, 2006; Zhang et al., 2006; Tang et al., 2019; Xu et al., 2019), the

tectonic and geological setting of the ore fields (Han et al., 2001, 2006, 2014). In these studies, these deposits in the SYG province have some common characteristics and are hosted in Sinian (Mesoproterozoic to early Neoproterozoic) to Permian (upper Palaeozoic) siliceous dolostones with orebodies controlled by thrust faults and fold structures. In addition, these deposits have generally very high ore grades with 25–35% Pb and Zn (up to 60%). They are spatially and chronologically related to the Emeishan basalts of the upper Permian (ca. ~260 Ma), while Sm-Nd isotopic studies of calcite suggested isochron ages of 226 ± 15 Ma and 225 ± 38 Ma for the Qilinchang and Kuangshanchang deposits, respectively (Zhou et al., 2002, 2018; Hu and Zhou 2012; Zhang et al., 2015). Recent geochronological studies using the Rb-Sr sphalerite dating technique (Tang et al., 2019), yielded an isochron age of 206.2 ± 4.9 Ma for the Yunleheba deposit, indicating that these ages are exceedingly younger than the flood basalts. The ore-forming fluids of these deposits are characteristic of low temperatures of 150–280 °C and low to moderate salinity of 4–15 wt% NaCl (Zhang et al., 2005; Han et al., 2007). Although studies of bulk and chemical compositions of sulphides are available, the origin of the deposit remains a subject of debate.

Mineral elemental analysis is an important tool in determining the petrogenesis, especially for understanding processes of ore formation (Cook et al., 2009, 2016; Large et al., 2009; Bonnet et al., 2016; Xiao and Li, 2019) and nature of ancient hydrothermal systems. Combined geology and trace elements data can aid such interpretation; for example, Cu, Ga, Ge, Cd, and Fe of sulphides from Mississippi Valley-Type (MVT) deposits (Cook et al., 2009; Pfaff et al., 2011; Ye et al., 2011; Bonnet et al., 2016; Wei et al., 2018); volcanic-hosted massive sulphide (VHMS) deposits (Genna and Gaboury 2015; Soltani Dehnavi et al., 2015, 2018; Basori et al., 2018; Leng et al. 2019); and trace elements in sphalerite from metamorphosed sulphide deposits (Lockington et al., 2014; George et al., 2016). Previous researches showed that some base metal sulphides could host a broad series of trace elements in mineral phases with complex texture and maybe substitutional in solid solution or occur as nano- to micro-scale inclusions. Trace/minor elements of sulphides can be used to determine deposit types and ore-forming temperatures (Frenzel et al., 2016).

Pyrite and sphalerite are both the common ore minerals and can occur in different stages of ore formation of carbonate-hosted MVT deposits, including the Qilinchang Pb-Zn deposit. Previous studies on trace element distributions in pyrite by electron microprobe (Abraitis et al., 2004; Reimold et al., 2004) and laser-ablation inductively coupled plasma mass spectrometry (LA-ICP-MS, Large et al., 2009, 2013, 2014; Koglin et al., 2010; Zhao et al., 2011; Cook et al., 2013; Gregory et al., 2015; Keith et al., 2016; Leng et al. 2019; Meng et al., 2019) have indicated that pyrite can contain minor elements such as Mn, Co, Ni, Cu, Zn, As, Se, Mo, Ag, Cd, Sb, W, Au, Hg, Tl, Pb and Bi by simple or coupled lattice substitution or as small sub-micron or nano-inclusions (Large et al., 1999, 2009; Reich et al., 2005, 2006; Barker et al., 2009; Cook et al., 2009, Deditius et al., 2009a, 2009b, 2011; Sung et al., 2009; Koglin et al., 2010; Ulrich et al., 2011; Basori et al., 2018). However, a number of reviews have also interpreted pyrite to contain minor elements up to the weight percentage level. On the other hand, sphalerite as the chief ore of zinc is one of the most common sulphide minerals found in the Qilinchang MVT deposits and has the potential to determine the temperature of formation. Despite its simple chemical formula (Zn, Fe)S, it preferentially incorporates several additional minor and trace elements into its tetrahedrally cubic crystal structure. A range of elements enter the sphalerite structure via simple cation exchange of bivalent equal-sized ions (e.g., $Zn^{2+} \leftrightarrow Fe^{2+}$, Cd^{2+}, Mn^{2+}, Hg^{2+}, Co^{2+}) or by coupled substitution mechanisms (e.g., $Zn^{2+} \leftrightarrow Cu^{+} + In^{3+}$). Several factors are responsible for the fractionation of a given element into sphalerite; amongst are; (a) crystallization temperature of the ore deposit, (b) metal source and, (c) amount of sphalerite in the ore. Grain-scale compositional zoning is identified in many sphalerites which are characterized by variations in Fe content. The incorporation

mechanisms of these elements in sulphides from the MVT deposits are lacking, whether these elements are incorporated in the sulphides either by simple/coupled lattice substitution including stoichiometric substitution in the instance of Ni, Co, Te and Se (Large et al., 2007) and non-stoichiometric substitution in the case of As, Au, Tl, and Mo; or as micro to nano-inclusions of elements of Zn, Cu, Ba, Pb, Bi, Ag and Sb (Deditius et al., 2011).

In this contribution, we describe the deposit geology and ore petrography, trace element compositions of pyrite and sphalerite, and present in-situ dataset from the Qilinchang Pb-Zn deposit, southwest China. This new dataset is interpreted to understand the incorporation mechanisms of these elements in sulphides and ore-forming processes of the deposit. The main objectives of this study are to evaluate the chemical variations of different generations of pyrite and sphalerite, unravel possible factors responsible for such variations, and eventually discuss the origin of the Qilinchang Pb-Zn deposit.

2. Geological setting

2.1. Regional geology

The SYG metallogenic province is located adjacent to the southwestern margin of the Yangtze Block (Fig. 1b; Zhou et al., 2018). The Yangtze Block is bounded to the west by the Sanjiang Block (SB), to the east by the Cathaysian Block (CB) and to the north by the Songpan-Ganzi Block (SGB). The block (Fig. 1a) is made up of Archean to the Proterozoic rocks and Palaeozoic to Mesozoic sedimentary strata (Zhou et al., 2002; Yan et al., 2003). The folded basement rocks in this region comprise of the Kangding, Dahongshan, and Kunyang Groups (Mesoproterozoic-Early Neoproterozoic). Lithologically, it is composed of tightly packed sandstones, slates, greywackes, shale, dolostone, and carbonaceous to a siliceous sedimentary sequence that is closely folded but weakly metamorphosed (Sun et al., 2009). The Mesoproterozoic to the Early Neoproterozoic rocks of the Kunyang Group are believed to have been formed in a foreland basinal setting. The overlying sedimentary cover which lies unconformably above the Kunyang Group is composed of Palaeozoic to Late Mesozoic strata of shallow marine origin, and clastic sedimentary stratigraphic units in a rifted continental slope and the late Triassic to Cenozoic strata of continental facies (Yan et al., 2003). The Sinian Dengying Formation consists of siliceous dolostone, argillaceous shale interbedded with sandy mudstone, which is conformably overlain by Early Cambrian Qiongzhushi Formation, mainly consist of argillaceous shale and sandy mudstone. This is followed by the deposition of sedimentary rocks of the Haikou and Zaige formations, mostly made up of fine-grained dolostone and argillaceous shale. Sedimentary rocks of Late Devonian are conformably lain atop by limestone and shale of Early Carboniferous Datang, Baizuo, and Weining formations, which are later conformably covered by Late Carboniferous Maping Formation that composes of breccoid limestone and shale. This is followed by the deposition of Early Permian Liangshan Formation containing fine-grained sandstone and argillite, which later in turn conformably overlain by Middle Permian Qixia-Maoku Formation, mainly composed of dolomitic limestone. This sequence is disconformably capped by Late Permian Emeishan basalt characterized by massive and localized amygdaloidal structures.

2.2. Deposit geology

The Qilinchang Pb-Zn deposit is situated above the Qilinchang fault, and it is made up of the Qilinchang and Dashuijing mining sections. The deposit is hosted mainly in dolostone of the lower part of the Early Carboniferous Baizuo Formation. The massive dolostone was formed as a result of extensive regional dolomitization, before the formation of the Qilinchang deposit. Overlying Carboniferous rocks are carbonaceous shale intercalated with fine-grained sandstone of the Liangshan Formation in the upper part and fine-grained sandstone interbedded
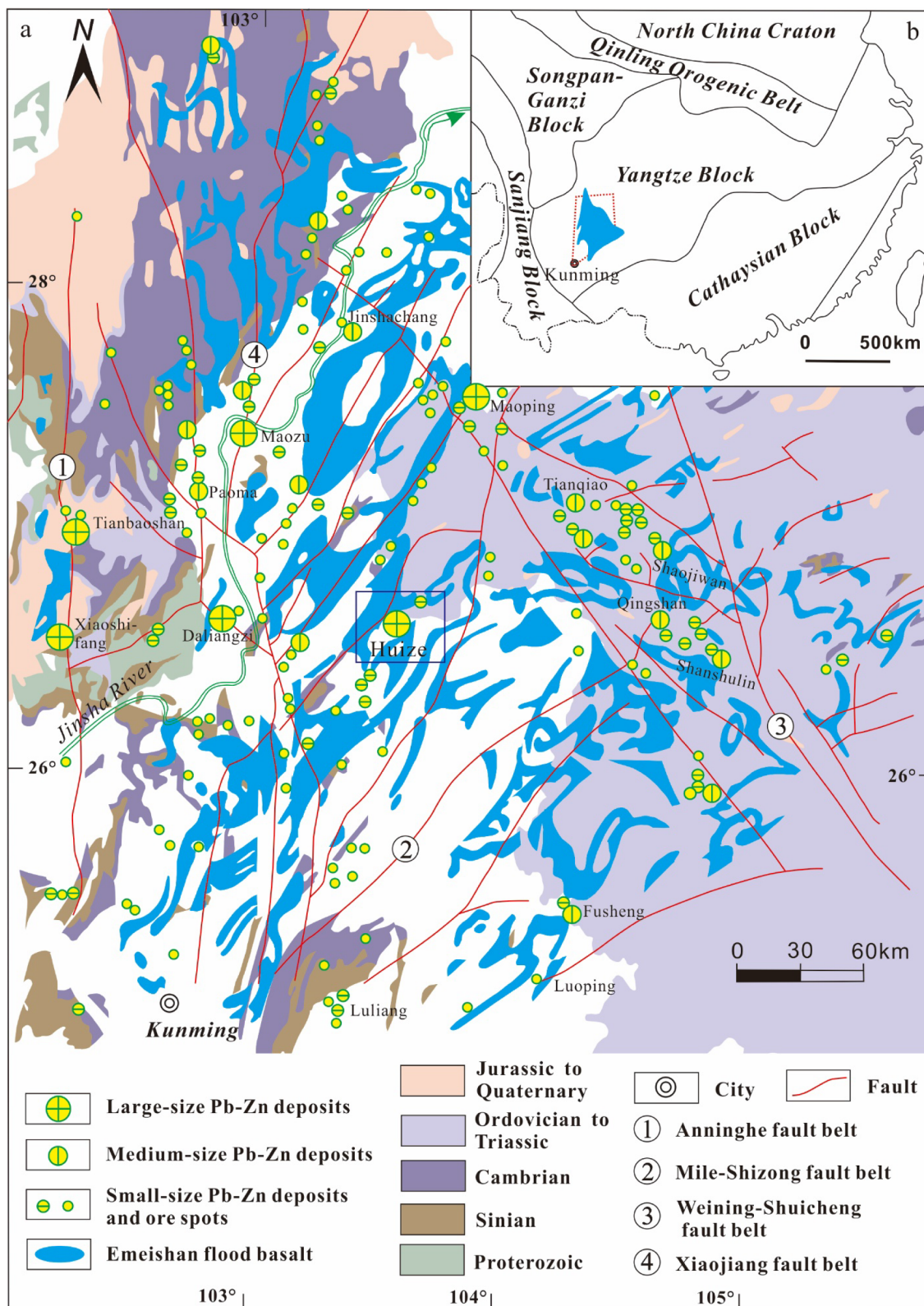
Fig. 1. (a) Simplified geological map of the Sichuan-Yunnan-Guizhou MVT triangle (after Zhang et al., 2015; Zhu et al., 2016). (b) Simplified tectonic map of South China (after Zhu et al., 2016).

with argillite in the lower section. Fold and fault structures in the Qilinchang Pb-Zn deposit are well developed, overarching the NE-trending Qilinchang and the Dongtou fault (Fig. 2). The Qilinchang-Dongtou thrust fault (F₁) trends N20˚–30˚E and steeply dipping S50˚–76˚E. This regional structure controls the formation and

localization of Pb-Zn deposits in the area. At the horizontal plane, ore bodies mostly occur as sheets, stratoids, veins, sacs, flat columns, or stockwork, whereas at the vertical plane, ore bodies are mainly present as lenticels, with thin and pinched branches at the top and tail end. Ore bodies in the Qilinchang deposit are predominantly composed of
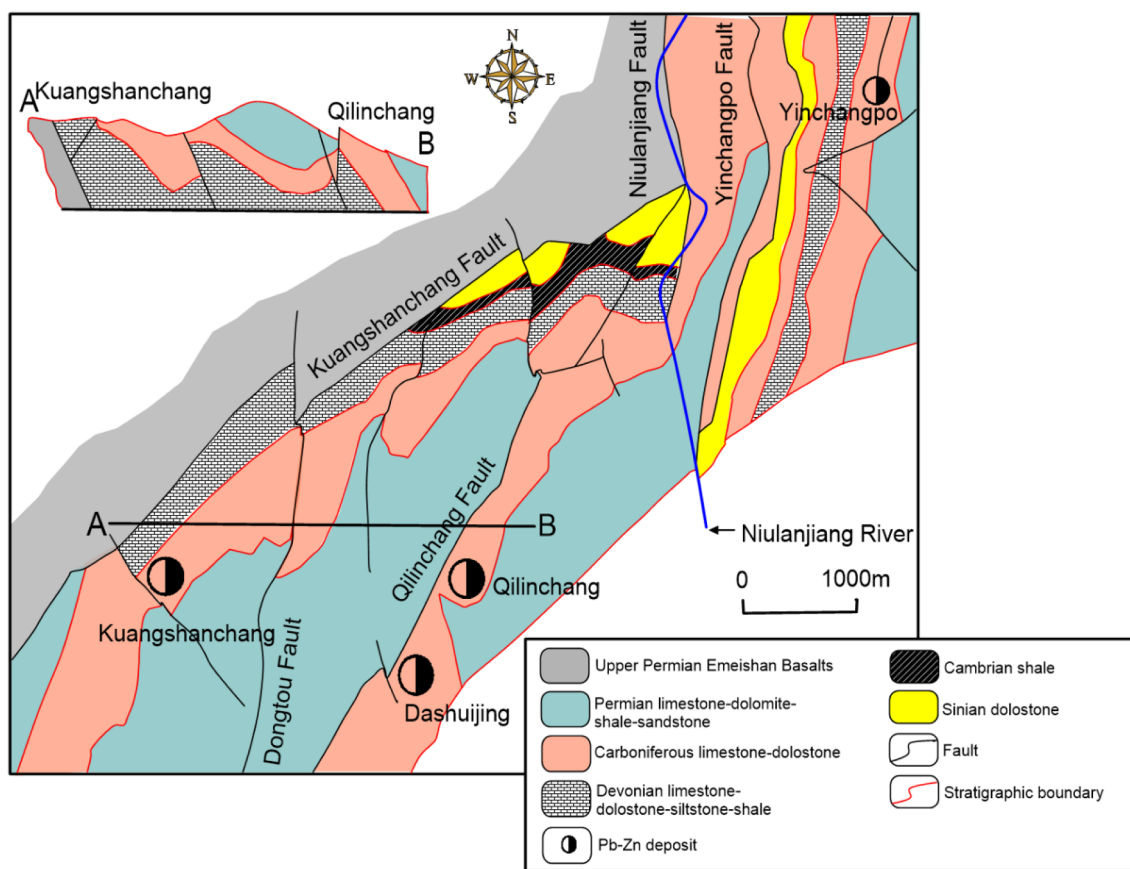
Fig. 2. Simplified geological map of the Huize deposit (Modified after Han et al., 2007).

massive, disseminated, banded, veined and brecciated ores. There are four ore bodies in the Qilinchang deposit, namely, No. 3, No. 6, No. 8, and No. 10 (Fig. 3), of which No. 8 is the largest. These ore bodies contain over 1.9 million tons Pb-Zn ores at grades of 2.3–9.2% Pb and 2.7–22.5% Zn, with high Zn/Pb ratios on the order of 5–14. There is also the minor occurrence of trace elements such as Ga, Ge, Cd, and Ag (Zhou et al., 2001; Han et al., 2007; Li et al., 2007; Yin et al., 2009). Mineralogically, sulphide ores are relatively simple and comprise mineral assemblages of sphalerite, galena, and pyrite with minor arsenopyrite, chalcopyrite, bornite, marcasite, and native antimony. Gangue minerals are mainly dolomite, calcite, and quartz.

2.3. Paragenetic sequence

Based on mineral assemblages and textures, the ores are present as disseminated, massive overgrowth, brecciated, fragmented, and replacement relics. The mineral paragenesis of the Qilinchang deposit can be divided into two periods: hydrothermal metallogenesis and supergene oxidation. The hydrothermal period is further divided into three metallogenic phases; pyrite-sphalerite stage, sphalerite-galena-pyrite stage, and pyrite-chalcopyrite stage (Fig. 4).

2.4. Mineral assemblage

The observed main textural characteristics of pyrite in the studied samples can be classified as; fine-grained pyrite (Py-I) corresponding to the pyrite-early sphalerite stage, medium-grained hydrothermal pyrite (Py-II) matching to the sphalerite-galena-pyrite stage, and coarse-

grained hydrothermal pyrite (Py-III) corresponding to the pyrite-chalcopyrite stage (Fig. 4). Py-I exists as irregular aggregates (5–50 μm), anhedral, cubic, disseminated pyrite crystals. Py-II is present as hydrothermal pyrite with anhedral-subhedral habits, and they are disseminated throughout the massive sulphide ores. Py-III also occurs as coarse-grained, pentagonal dodecahedron crystal hydrothermal pyrite (50–1500 μm), and subhedral-euhedral crystals. Pyrites are present as an anhedral to subhedral medium-grained crystals that exist in solid solution (Fig. 5a, c, d, f, g, i and 6a, c, f, g, h, i). In contrast, massive crystals of pyrite are fractured, display cataclastic texture and stress deformation (Fig. 5a–c, e). At places, calcite also shows centimeter-scale vein intruding into massive, less fractured crystals of Py-II and Sph-I (Figs. 5c, 6b). Calcite also exhibits replacement texture with Py-I and Py-II (Fig. 5e). Galena is subhedral to anhedral, fine-grained forms replacement minerals (Figs. 5b, f, g, h and 6c, d, e), also shows millimeter-scale fragments of a crystal (Fig. 6b) associated with veins of calcite. Sphalerite is present as euhedral-subhedral fine-grained crystals coexisting with galena (Fig. 6b). However, marcasite occurs as a bladed structure confined within a groundmass of Sph-II associated with coarse-grained galena (Fig. 6d). In addition, pyritohedral-shaped and fractured relics of Py-III display oscillatory zoning and associated with galena and dolomite (Fig. 6f, g, h, i).

Two types of sphalerite were outlined based on the paragenetic sequence and colour as follows: (a) early dark-brown sphalerite (Sph-I) formed during the Stage I and associated with galena, minor pyrite, and ferrodolomite (Figs. 5d, f, 6a, b, c, d). These sphalerites are present as euhedral to subhedral fine-grained crystals and commonly indicate intergrowth with early-stage pyrite (Py-I) and galena (Gn-I), forming
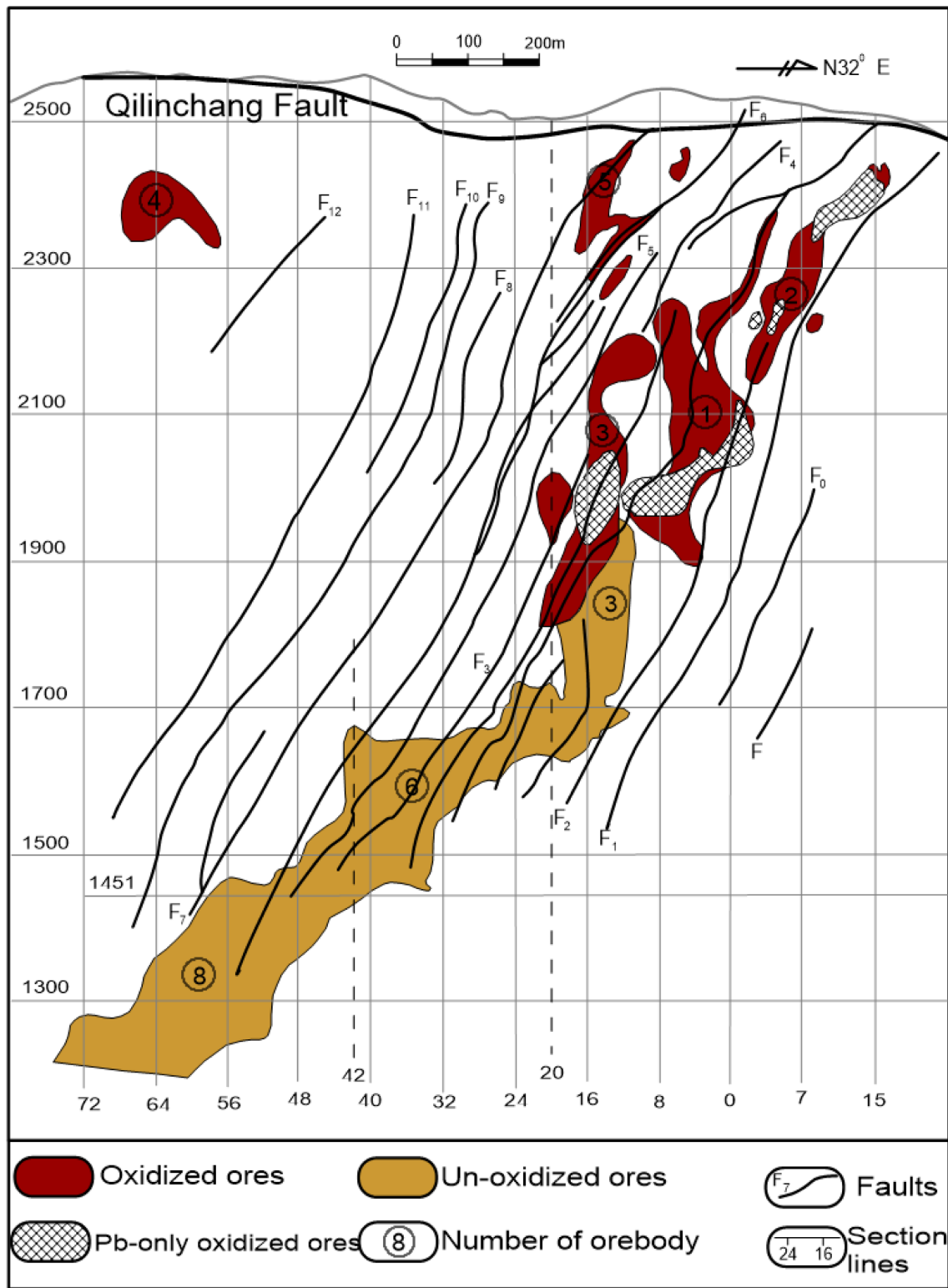
Fig. 3. The vertical projection of the Qilinchang Pb-Zn-(Ag-Ge) deposit in the Huize district.

embayment texture. (b) late light-yellow sphalerite (Sph-II) developed stage II, widely distributed throughout the massive ores and breccia-type ores (Figs. 5f, g, h, 6c, d). These crystals appear as euhedral to subhedral fine-grained crystals coexisting with Py-II and Dol-II. They exhibit compositional zoning, which displays the alternation of sphalerite layers.

3. Analytical methods

3.1. Sampling

Representative ore samples were collected systematically at stope 8# of tunnel 1237 m. These samples provided the subsurface geological information explained in this research. Sampling was conducted along a

Minerals \ Stage	Diagenetic processes	Hydrothermal mineralization			Supergene alteration
		Stage-I	Stage-II	Stage-III	
		Py-Sph	Sph-Gn-Py	Py-Ccp	
Pyrite	▬	Py-I	Py-II	Py-III	
Sphalerite		Sph-I	Sph-II		
Galena			▬	▬	
Marmatite		▬			
Chalcopyrite				▬	
Acanthite			▬		
Chlorargyrite					▬
Freibergite			▬		
Matildite			▬		
Dolomite	▬	▬	▬	▬	
Calcite	▬	▬	▬	▬	
Quartz				▬	
Barite					▬
Gypsum	▬				▬
Fe-hydroxides					▬
Hopeite					▬

Fig. 4. Mineral paragenesis in the Qilinchang Pb-Zn deposit (Modified after Han et al., 2007).

broad range of geological cross-sections to obtain suitable rock samples for petrological and geochemical analyses. Subsurface and deposit scale geological maps and sections were provided for this study by the site geologists and technicians of the Qilinchang Pb-Zn mine.

3.2. LA-ICP-MS analyses

LA-ICP-MS analyses were carried out using the 193 nm Microlas Pro ArF Excimer coupled to an Agilent 7500c quadrupole mass spectrometer at the State Key Laboratory of Ore Deposit Geochemistry, Chinese Academy of Sciences. Spots of interest within each sample were pre-selected under the Scanning Electron Microscope (SEM) to detect micro inclusions or inhomogeneity in sample composition that could affect the quality of the data. Ablation was performed using a uniform spot diameter of 24 μm, a 5 Hz laser pulse rate, and 80–85% power level. The analytical procedures for the laser ablation and calibration are described in Lach et al. (2013), and Belissont et al. (2014). The following isotopes were measured ^{25}Mg, ^{27}Al, ^{29}Si, ^{34}S, ^{39}K, ^{43}Ca, ^{45}Sc, ^{49}Ti, ^{51}V, ^{53}Cr, ^{55}Mn, ^{57}Fe, ^{59}Co, ^{60}Ni, ^{65}Cu, ^{66}Zn, ^{71}Ga, ^{74}Ge, ^{75}As, ^{77}Se, ^{85}Rb, ^{88}Sr, ^{95}Mo, ^{107}Ag, ^{111}Cd, ^{115}In, ^{118}Sn, ^{121}Sb, ^{184}W, ^{196}Pt, ^{197}Au, ^{202}Hg, ^{205}Tl, ^{208}Pb and ^{209}Bi. The total 90 s analysis time included a 25 s background measurement before ablation. Instrument calibration was done using the QC-MASS-1 trace element standard. The data reduction was employed with the use of Glitter software. The Fe and Zn concentrations values determined by Electron Probe Microanalysis

(EPMA) were used as an internal standard for the pyrite and sphalerite analysis, respectively. Multiple standard analysis (FeSb, GSD-1G, GSE-1G, and Py) were run at the beginning and end of each sequence of 10 unknown samples to correct instrument drift.

3.3. Image analysis

Element maps were produced by ablating sets of equally parallel lines across the pyrite and sphalerite grains using a consistent 15 μm beam size, line spacing of 15 μm, and 25 μm/s scan speed at a laser frequency of 10 Hz and 0.003 s dwell time for all elements. Identical rasters were performed on the MASS-1 reference material at the beginning and end of a mapping run to correct instrumental drift. Element maps were compiled and processed using the program Iolite (Woodhead et al., 2007), and Igor developed by WaveMetrics. The average background intensity of every element was deducted from its corresponding raster, the resultant time-resolved intensities compiled into a 2D image displaying both background/drift corrected intensity for each element combined using a logarithmic colour scale (Cook et al., 2013).

3.4. Principal component analysis of in-situ datasets

Principal component analysis (PCA) is a multivariate technique used to emphasize variation and bring out strong patterns in a dataset. PCA
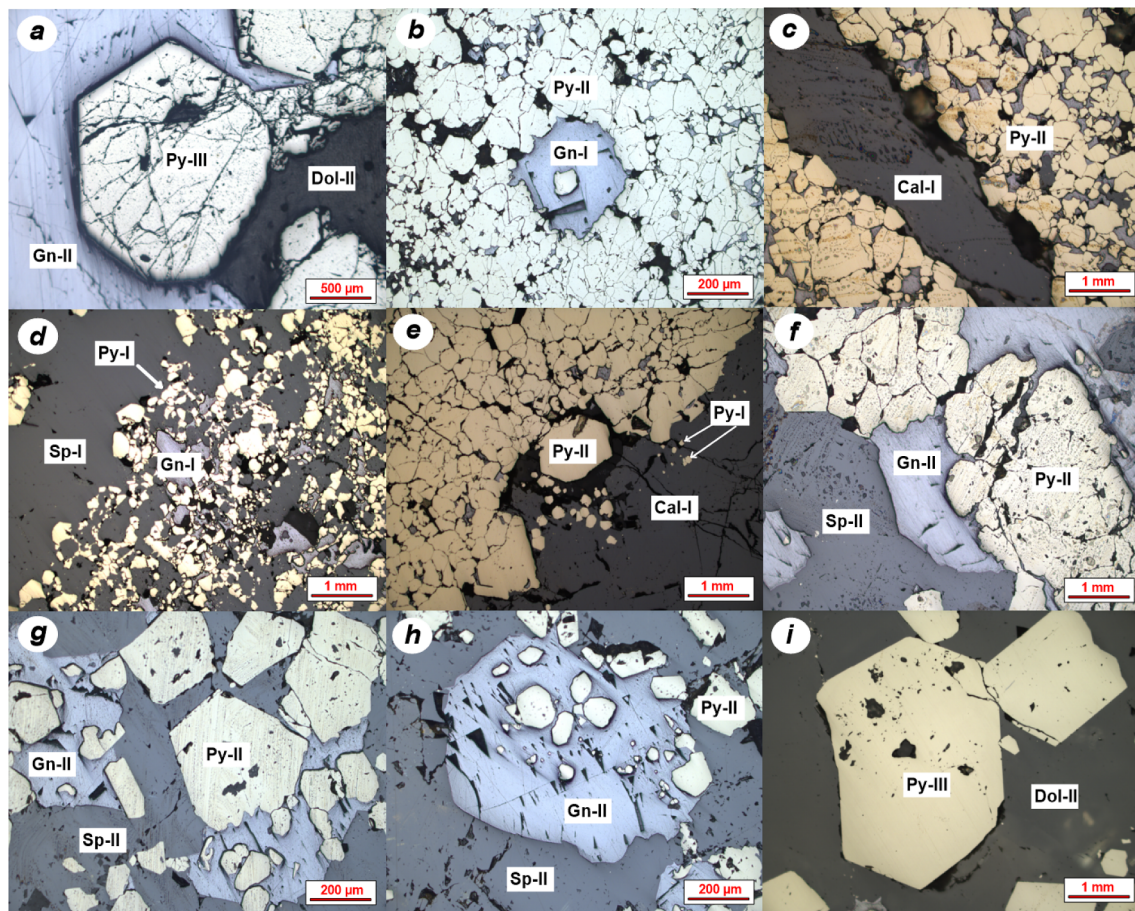
Fig. 5. The textural and structural characteristics of sulphides and associated gangue minerals in the Qilinchang deposit viewed under the microscope; (a) pyrite (Py-III) occurs as euhedral to subhedral coarse-grained crystals and coexist with galena (Gn-II) and dolomite (Dol-II); (b) subhedral, fine-grained galena (Gn-I) replaced by spongy pyrite (Py-II); (c) anhedral, fine-grained disseminated Py-II cross-cutted by calcite (Cal-I), Cal-I forms a veinlet along fractures within the pyrite crystal; (d) pyrite (Py-I) occurs as disseminated and isolated fine-grained aggregates of anhedral crystals within a groundmass of sphalerite (Sp-I), observed galena of stage-I is replaced by pyrite; (e) Cal-I been replaced by composite aggregate of isolated and spongy pyrite of Py-I and Py-II respectively, the massive crystal of Py-II is highly fractured; (f) Py-II occurs as euhedral to anhedral, coarse-grained crystals replacing Gn-II and coexist with sphalerite (Sp-II) in solid-solution; (g) euhedral, coarse-grained elongated Py-II associated with Sp-II and irregular shape Gn-II; (h) fine-grained, euhedral-subhedral galena crystals enclosing relicts of Py-II, all of which are enclosed by Sp-II; (i) medium-grained, euhedral Py-III crystals enclosed by Dol-II.

can also be used for the identification of a smaller number of un-correlated variables from a larger set of data. It is a simple non-parametric statistical technique for extracting information from complex datasets, is focused on the maximum variance amount with the fewest number of principal components (PCs). It is closely related to canonical correlation analysis but uses the orthogonal transformation to convert the set of observations containing correlated variables into a set of values known as principal components. PCs are determined by maximizing the variance and later ranking them in terms of magnitude with a negative correlation. The main advantage of PCA is that the data sets can be compressed (i.e., by reducing the number of dimensions), without much loss of information (Frenzel et al., 2016). PCAs are expressed as eigenvectors and corresponding eigenvalues of the covariance matrix of the data points, and the eigenvectors are sorted according to their eigenvalues in decreasing order. The highest variance relating to the most significant correlation between the variables can be obtained and presented in the form of numbers and histograms. The most important application of PCA is that it can be widely applied in the domain of geochemical exploration on large-scale data sets (Samama et al., 1989), which may provide information on the underlying ore mineralization and its organization. Also, PCA has been used in sulphide geochemistry (Winderbaum et al., 2012) and isotope geochemistry (Iwamori et al., 2010; Belissont et al., 2014).

In this study, *in situ* minor/trace elements data were log-transformed and processed by the PCA program included in the OriginPro software. Finally, we generate principal components, whose eigenvectors and eigenvalues provide the enrichment attributes of the *in-situ* LA-ICP-MS datasets in our study.

4. Results

4.1. LA-ICP-MS results

The trace element concentrations of pyrite and sphalerite were determined by LA-ICP-MS. A total of 175 LA-ICP-MS spot analyses ablated for this study is representative of the three mineralizing stages delineated from the Qilinchang deposit. The summaries of the results of the pyrite analyses, which include forty-nine ablations for Py-I, fifty-four for Py-II, and seventy-two for Py-III are listed in Table 1, while the representative time-resolved depth profiles and complete data are presented as Supplementary data S1 and S2 respectively.

Py-I is enriched in Mg, Mn, Co, Ni, and Tl compared to other pyrite stages (Table 1). The concentrations of Au (average 0.11 ppm) and Bi (average 0.21 ppm) are relatively low in Py-I. A distribution pattern of elements from ablated spots of Py-I is shown in Fig. 7a. The trend of these elements such as As, Zn, Ge, Cd, Ni, Tl, Mn, Cu, Se, Sb, and Pb, indicate that these trace elements are present within the lattice structure of Py-I or as evenly distributed micro- to nano-inclusions.
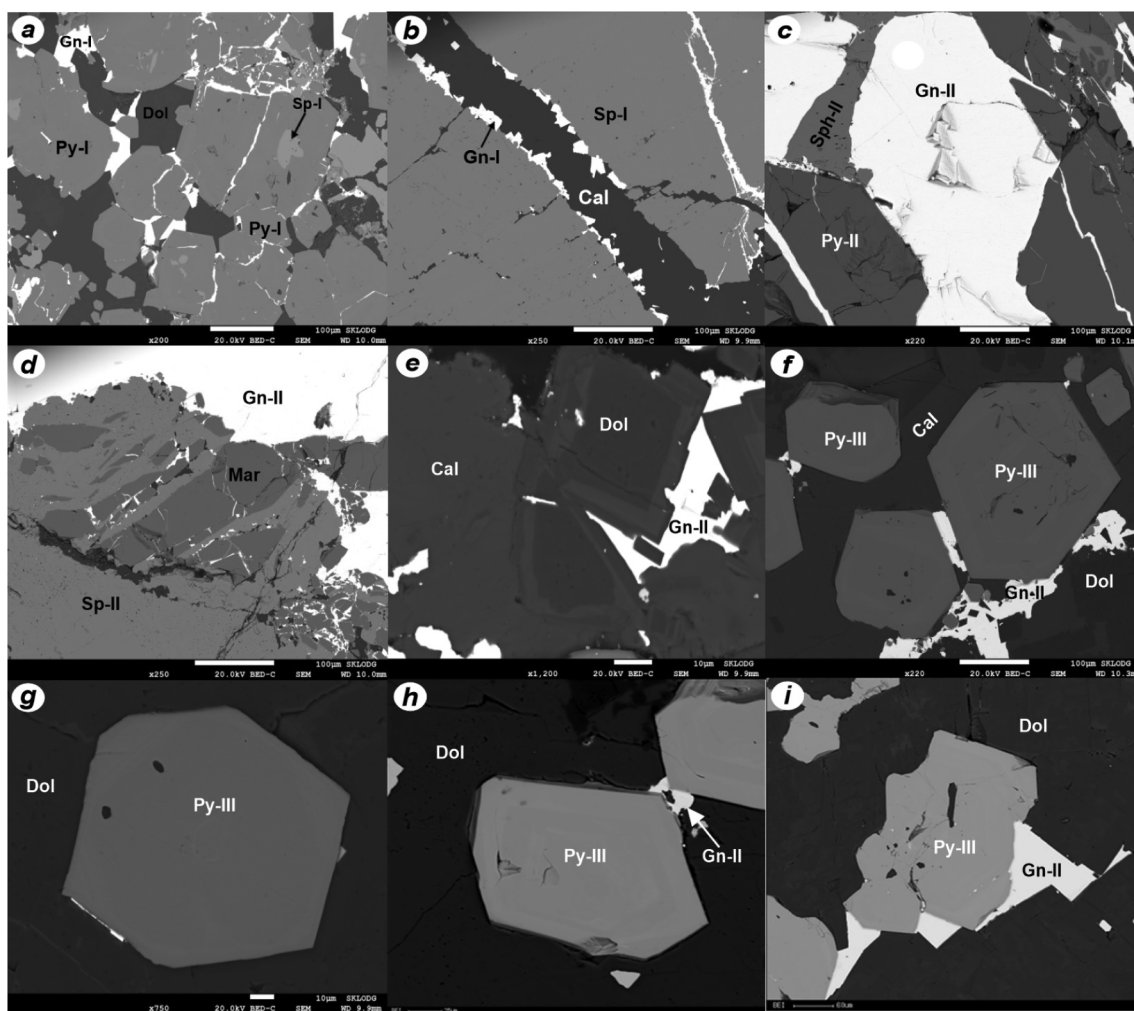
Fig. 6. SEM-BSE images of polished sections illustrating the texture and structure of hydrothermal minerals in the Qilinchang deposit; (a) sphalerite (Sp-I) occur as subhedral fine-grained crystals enclosed within the early stage pyrite (Py-I), coexisting with galena (Gn-I), all of which form embayment texture with dolomite (Dol), Gn-I are enclosed by Dol and forms fine veinlets and fill fractures in the pyrite (Py-II); (b) Sp-I present as euhedral-subhedral fine-grained crystals coexisting with Gn-I, both of which are intruded or filled a fracture in Sp-I with calcite (Cal) forming solid-solution; (c) Py-II occurs as coarse-grained crystal coexist with fine-grained sphalerite (Sp-II) and coarse-grained galena (Gn-II); (d) bladed marcasite (Mar) enclosed within a groundmass of Sp-II associated with coarse-grained Gn-II; (e) Gn-II coexists with Cal and Dol; (f) pyrite (Py-III) present as euhedral medium-grained crystals coexist with Gn-I at the edges of the rims of pyrite, all enclosed by Dol and Cal solid-solution; (g) euhedral, medium-grained Py-III, enclosed within a groundmass of dolomite; (h) cubic Py-III display oscillatory pattern and associated with Gn-II and Dol; (i) Gn-II occur as subhedral fine-grained crystal displaced by Py-III, both of which are surrounded by Dol in solid-solution.

Py-II is enriched in Cu, Zn, Ga, Ge, As, Se, Mo, Ag, Cd, In, Sn, Hg, and Sb compared to other pyrite types (Table 1). The concentrations of V (average 16.34 ppm) and Cr (average 29.21 ppm), are most likely present in small rutile or other Fe-Ti oxide inclusions within the pyrites. The mean values of Cu (average 11,426 ppm), As (average 3717 ppm), Ag (average 1016 ppm and Bi (average 14.59 ppm) are significantly higher in Py-II relative to Py-I (Table 1). The distribution profile for Py-II (Fig. 7b) and elements of As, Zn, Ge, Cd, Ni, Tl, Mn, Cu, Se, Sb, and Pb indicate that they are mostly contained within the crystal lattices of the Py-II structure.

The concentrations of trace elements in Py-III are variable, but more enriched in elements of Ti, V, Cr, Pb, and Bi compared to Py-I (Table 1). The box and whisker plot show (Fig. 7c) variable distribution of Cu, As, Ni, Ag, and Pb compared to Py-I and Py-II. This indicates that the elements, especially Ag and Pb, occur as micro mineral inclusions of galena as observed from the generated LA-ICP-MS time-resolved depth profile.

A total number of 119 LA-ICP-MS spot analyses were ablated for this study, and these are representative of the two types of sphalerite present in the Qilinchang deposit. The summaries of the results are presented in Table 2, with seventy-nine spots accounted for Sph-I, and forty spots assigned to Sph-II. Sph-I is more enriched in Mn, Fe, Co, Ni, Cu, Ga, Ge, As, Ag, Cd, In, Sb, Hg, and Pb relative to stage-II sphalerite. Sph-I displays significantly elevated concentrations of Fe and Cd (average 170,055 ppm and 1065 ppm), respectively. These are enriched in the dark-banded growth zones. On the other hand, Cu, As, and Hg exhibit a wide range of concentrations (5.42–6783 ppm, limit of detection to 7280 ppm and 77–5600 ppm), respectively. Besides, Ge, Sn, and Tl show a similar range of concentrations in the two sphalerite types. In the same way, both Sb and Ag reveal similar distributions (0.05–538 ppm and 1.57–525 ppm), respectively, but have lower values in Sph-II with average concentrations of 7.14 and 9.12 ppm, respectively. Sph-II have lower concentrations in almost all elements compared to Sph-I (Table 2). The contents of Sb and As also show indicate distribution (0.02–118 ppm and 0.09–112 ppm), respectively. Almost all elements analyzed in exception of those whose concentrations are below the limit of detection, such as elements of Cd, Ge, Hg, Mn, and Zn detected in the samples are homogeneously distributed, while Fe, Cu, Ag, Ga, In, Pb, and Sb are zoned.

Table 1
Summary of trace/minor element concentrations (ppm) of different generations of pyrite from the Qilinchang Pb-Zn deposit, Southwest China.

Element	Py-I (n = 49)				Py-II (n = 54)				Py-III (n = 72)			
	Min	Max	Mean	1σ SD	Min	Max	Mean	1σ SD	Min	Max	Mean	1σ SD
Ti	28.69	1505	97	230	6.96	3237	292	619	< LOD	55,316	882	6517
V	0.07	6.79	0.6	1.50	< LOD	650.4	16.34	89	< LOD	3350	48	394
Cr	0.4	60.24	3.24	9.34	< LOD	535.0	29.21	92.02	< LOD	1283	42	157
Mn	0.23	126,900	2700	18,120	< LOD	45,506	2313	6570	< LOD	3660	317	616
Co	0.02	31.81	5.21	8.14	< LOD	22.9	2.17	4.34	< LOD	19.89	1.25	3.61
Ni	0.1	487	47	92	< LOD	194.1	11.98	29.38	< LOD	64.02	5.30	11.35
Cu	0.28	4935	164	739	0.47	181,722	11,426	36,362	0.06	108,327	3795	17,092
As	27.32	21,796	2200	4741	< LOD	40,153	3717	7128	< LOD	13,855	958	1934
Se	1.29	207	10	29.82	< LOD	1756.3	101	321	< LOD	381	13.40	46.83
Mo	0.02	6.83	0.46	1.33	< LOD	21.1	2.01	4.59	< LOD	13.84	0.92	2.25
Ag	0.03	39.85	3.08	6.83	0.15	18,865	1016	2749	< LOD	19,596	568	2370
Sb	0.03	540	39	96	0.58	23,596	1522	4804	0.15	17,700	439	2100
Au	0.02	3.51	0.11	0.50	< LOD	6.7	0.46	1.10	< LOD	1.72	0.17	0.34
Tl	0.02	17.09	1.01	3.40	< LOD	0.8	0.05	0.15	< LOD	1.84	0.11	0.32
Pb	0.03	8122	710	1670	< LOD	897,183	17,809	122,049	< LOD	3,920,720	133,770	620,566
Bi	0.01	2.39	0.21	0.49	< LOD	472	14.59	64.49	< LOD	1054	76.15	182

1σ SD: standard deviation.
LOD: limit of detection.

4.2. Image analysis

In addition to the spot analyses, LA-ICP-MS element maps were generated for trace elements present in the pyrite-sphalerite assemblage. This provided insights into the element partitioning ability among the sulphides. The first set of images of Py-I (Fig. 8) associated with gangue mineral displays an elongate and anhedral to subhedral pyrite structure. In this sample As, Fe, and Ge are preferentially enriched in the core of pyrite while Ag, Co, Cr, Cu, Mg, Mn, Ni, Pb, S, Sb, Sn, and V are depleted in the core relative to the rim.

The second set of images of Py-III (Fig. 9) associated with the dolomite exhibit clearly outlined core and rim compared to Py-I. The cubic-shaped pyrite crystal displays sector zoning and is enriched in Cu, Pb, and Sb, while As, Co, and Ni exhibit a combination of oscillatory and sector zoning at the core. The distribution of other trace elements mapped is predominantly variable. Py-III contain Ag, and Pb as micro mineral inclusions.

The LA-ICP-MS element maps for sphalerite show compositional zoning between the dark-brown and light-yellow sphalerite bands (Fig. 10). Sph-I, which corresponds to the early formed stage, is enriched in Fe, Cu, Ag, Mn, Pb, and Sn, whereas there are variable concentrations of Cd, Ga, Ge, and Hg. This image highlights the distribution of trace elements incorporated between the lattice.

4.3. Principal component analysis of minor and trace elements

The PCA results applied to the LA-ICP-MS dataset for pyrite and sphalerite are presented in Figs. 14 and 15, respectively. Elements and spots analyses of pyrite representing the three mineralizing stages are projected on the PC1 *vs.* PC2 plane, which accounts for 63.4% of element content variability (Fig. 14a). Element distributions denote two main groups or element correlation clusters. PC1 accounts for 49.16% of element content variability including V, Mn, Cu, Zn, Se, Mo, Ag, Sb, Au, and Bi (loading PC1; Fig. 14b), whereas PC2 accounts for 14.24% of element content variability (Fig. 14a) is composed of As, Ni, and Co (loading PC2; Fig. 14b). Representative spots in the PC1 *vs.* PC2 plane (Fig. 14c) highlights the element enrichment characteristics in the mineralizing stages of pyrite (Fig. 14d). PC1 (loaded by V, Mn, Cu, Zn, Se, Mo, Ag, Sb, Au, and Bi) is correlated with the spots in Py-II and partly overlap with Py-III, whereas PC2 (loaded by As, Ni, and Co) is correlated with Py-I.

For sphalerite, the elements and spot analyses representing the two mineralizing stages are projected on the PC1 *vs.* PC2 plane, which

accounts for 60.57% (Fig. 15) of element content variability. Element distributions show two main groups. PC1 accounts for 40.87% of element content variability (Fig. 15a) including two subgroups (Fe, Cd) and (chalcophile elements of Ge, Cu, As, Sb and Ag) (loading PC1; Fig. 15b), while PC2 accounts for 19.70% of element concentration variability (Fig. 15a) is composed of In, Sn, and Ga (loading PC2; Fig. 15b). Spot presentation in the PC1 *vs.* PC2 plane (Fig. 15c) indicates element enrichment features in the mineralizing stages of sphalerite (Fig. 15d). PC1 (loaded by chalcophile and siderophile elements of Ge, Cu, As, Sb, Ag, Cd, and Fe) is correlated with the spots in Sph-I and partly overlap with Sph-II, while PC2 (loaded by In, Sn, and Ga) is primarily correlated with Sph-II.

5. Discussion

5.1. Pyrite textures and geological significance

Three main types of pyrite textures were identified from the Qilinchang Pb-Zn deposit. Py-I displays sector zoning, Py-II exhibits massive overgrowth texture, while Py-III shows replacement relics and a combination of oscillatory and sector zoning. These primary textures are interpreted as products of mixing of hydrothermal fluids of varying compositions or likely dissolution and recrystallization under a certain range of redox conditions (Deditius et al., 2011). The zoning characteristics of pyrite show an inclusion-rich core and depleted-rim. The sector zones are enriched in Ni, Cu, Pb, and Sb (Figs. 8 and 9). Massive, subhedral pyrite is probably formed as a result of the relative rapid nucleation process (Scott et al., 2009). Relics of pyrite formed in the late stage of the ore-forming process are also formed due to the replacement by dolomite or calcite. The compositional variation of trace elements in pyrite can be attributed to variable physicochemical conditions of ore-forming fluids during the crystallization of pyrite (Reich et al., 2005).

5.2. Incorporation and distribution of trace elements in pyrite and sphalerite

The common ore mineral present in the different stages of ore formation of the Qilinchang Pb-Zn deposit is pyrite, followed by sphalerite and galena. Major elemental variations of pyrite and sphalerite in the Qilinchang Pb-Zn deposit are primarily caused by mineral inclusions, co-precipitation of minerals, variation in the fluid composition, and physicochemical conditions of ore-forming fluids (Reich et al., 2005, 2013). Trace and minor elements can be incorporated into sulphides by
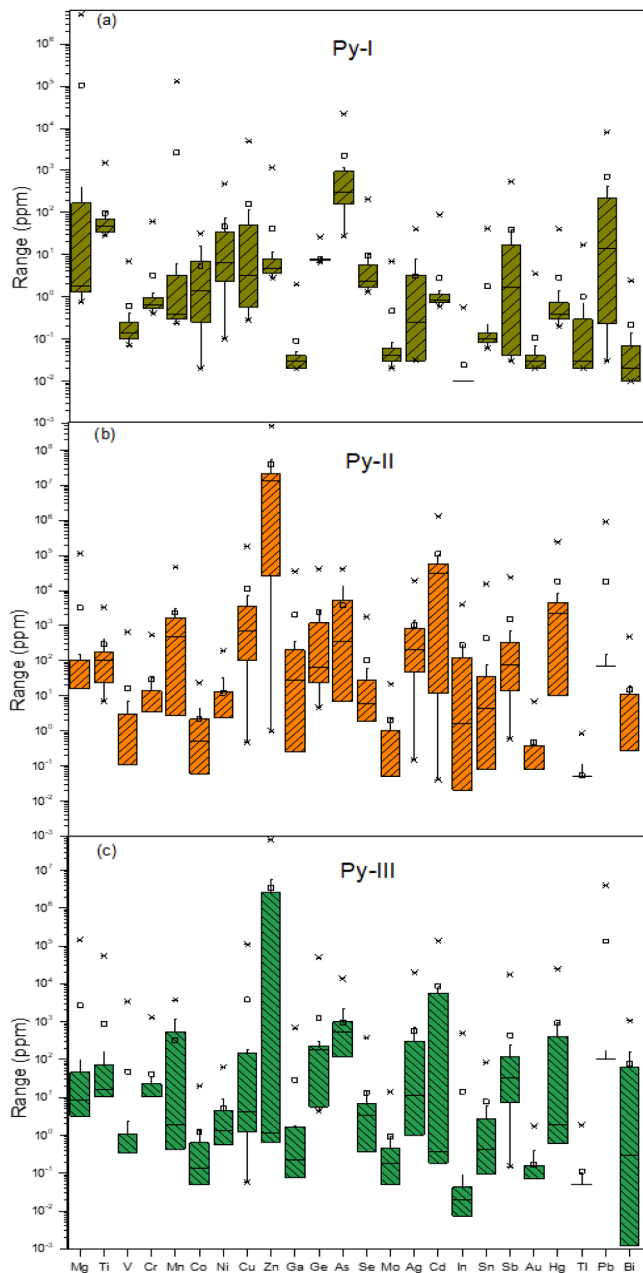
Fig. 7. Box and whisker plots are showing the ranges and averages of trace element compositions in (a) Py-I, (b) Py-II, and (c) Py-III, respectively from the Qilinchang deposit. Trace elements are presented in order of atomic number. The coloured boxes for each element represent the 25% to 75% data ranges. The horizontal lines in each box represent the minimum and maximum values for each element (ppm), the square symbol indicates the mean, while star symbol represents the 1% and 99% percentile for each element.

any of these three modes: (a) those that occur in mineral deposit as mineral phases, forming intergrowth textures and components of minerals in solid solution (Zhang et al., 2013), (b) those absorbed as impurities on surfaces of other minerals as micro- to nanoparticles of sulphides (Ciobanu et al., 2012) and (c) those absorbed as impurities on surfaces of other minerals as micro- to nanosized inclusions of silicate or oxide minerals (Thomas et al., 2011). Based on the distribution pattern and scatter graphs (Figs. 7 and 12), pyrite and sphalerite present in the paragenetic stages exhibit similarities and variations in element concentrations, as discussed below.

5.2.1. Controls on trace element concentrations of pyrite

As discussed earlier, pyrite occurs in the mineralization stage as fine-grained irregular aggregates of cubic, disseminated pyrite crystal; medium-grained hydrothermal massive, spongy, anhedral-subhedral crystal; and as medium-grained late hydrothermal, subhedral-euhedral crystal. These varied morphologies exhibit discernable trace elements concentrations, which are evidently related to hydrothermal fluid responsible for the mineralization (a function of temperature, pH, and/or fO_2).

Py-I occurs as fine-grained, micro-sized, cubic, disseminated pyrite, formed in the early stage of the paragenetic sequence, which is considered to have been developed from rapid mixing of ore-forming fluids of different concentrations or likely dissolution-reprecipitation under certain range of redox conditions (Deditius et al., 2011; Keith et al., 2016). The enrichment of Mg, Mn, Co, Ni, and Tl (Fig. 7a), indicate that these elements are incorporated within the lattice structure or as evenly distributed micro- to nano-inclusions. These findings are similar to those presented by Deditius et al. (2011), who analyzed nano-scale "liquid" inclusions of As-Fe-S in arsenian pyrite from low-temperature ore deposits, which is attributed to clustering of metals from hydrothermal fluids during precipitation. The concentration of metals precipitated together with the formation of colloform pyrite probably depicts such a trace element enrichment law. However, the enrichment of Mn in the pyrite indicates a relatively oxygenated sub-alkaline seawater environment as a result of lower temperatures (Deditius et al., 2011). Consequently, the presence of Tl in pyrite has been documented in some polymetallic deposits (Fan et al., 2014), suggests that Tl may isomorphically replace Fe in the pyrite structure where the content of Tl is relatively low (< 2000 ppm; Fan et al., 2014). At elevated concentrations, the variation in ionic radius between Tl^+ and Fe^{2+} constrain the formation of Tl-bearing minerals (e.g. Lorandite: $TlAsS_2$, Fangite: Tl_3AsS_4, Thalcusite: $Tl_2Cu_3FeS_4$, and Crookesite: $Cu_7(Tl, Ag) Se_4$).

Py-II occurs as massive, disseminated, and banded aggregates, evenly distributed mainly within the host rock adjacent to the orebodies. They typically display primary colloform and overgrowth textures that are dissonant to the main tectonic fabric. The concentrations of Cu, As, Se, Mo, Ag, and Sb are higher compared to Py-I and Py-III (Table 1). As shown in Fig. 7b, only a few elements such as As, Sb, Cu, Se, Mo, and Ag indicate identified inclusions and seems to increase compared to Py-I and Py-III. All these concentrations features show that Py-II exists as a phase between Py-I and Py-III and that the composition of the ore-forming fluid increased in a gradual pattern compared to low and variable concentrations in Py-I and Py-III respectively.

Py-III occurs as medium-grained, euhedral-subhedral hydrothermal pyrite, exhibiting sector and oscillatory zoning of cores and rims mostly present within dolomite in the hanging wall or fault zones near the orebodies. They are dominated by crystal sizes with pyritohedral-dodecahedra shape. The relatively elevated contents of Ti, V, Cr, Zn, Pb, Bi, and Ag in Py-III (Fig. 7c) shows micromineral inclusions of elements of Ag and Pb possibly constrain the formation of Ag-Pb and Ag-Bi bearing phases (e.g., matildite and/or galena). This group of trace elements was considered to be precipitated in the low-temperature regime (Han et al., 2007). Lead is least likely to be incorporated into the pyrite lattice due to its ionic sizes, but it has a faster rate of precipitation from basinal fluids as metal sulphide compared to Fe (Koglin et al., 2010). Also, Pb always forms PbS prior to pyrite precipitation, and galena inclusions in pyrite are common, as observed in this study (Table 1). Ag-Bi-Pb usually enters the pyrite lattice as inclusions of Ag-bearing minerals because Bi and Ag readily substitute into the structure of galena and may be present for element balancing. A number of few spots analyzed display the distribution of Cu in pyrite as chalcopyrite inclusions, as shown in Fig. 7c.

5.2.2. Mode of distribution of Au in pyrite and its possible genesis

The mode of distribution of trace elements, most importantly Au in the pyrite remains inconclusive, mainly due to the low spatial

Table 2

Summary of trace/minor element concentrations (ppm) of different generations of sphalerite from the Qilinchang Pb-Zn deposit, Southwest China.

Element	Sph-I (n = 79)				Sph-II (n = 40)			
	Min	Max	Mean	1σ SD	Min	Max	Mean	1σ SD
Mn	4.59	233	43.11	47.11	6.00	27.85	10.48	3.48
Fe	856	944,943	170,055	234,080	144	16,352	8292	4516
Co	< LOD	6.21	0.21	0.80	0.02	0.05	0.02	0.007
Ni	< LOD	94.15	2.87	10.97	0.1	0.27	0.13	0.03
Cu	5.42	6783	378	890	1.48	685	61.36	117
Ga	< LOD	321	11.83	44.48	0.01	89.63	7.88	15.94
Ge	0.13	325	35.17	58.63	0.08	205	18.53	36.24
As	< LOD	7280	281	1210	0.09	112	4.45	18.79
Ag	1.57	525	48.60	88.52	0.56	49.25	9.12	10.64
Cd	695	1774	1065	263.32	630	1608	830	174
In	< LOD	38.11	2.88	7.51	< LOD	9.43	0.75	2.06
Sn	< LOD	16.95	1.59	3.20	0.06	17.36	1.67	3.64
Sb	0.05	538	33.32	79.19	0.02	118	7.14	20.74
Hg	77	5600	476	1030	12.76	744	176	275
Tl	< LOD	0.55	0.03	0.07	0.01	0.05	0.02	0.01
Pb	< LOD	485	27.31	81	0.01	52.06	5.40	10.08
Bi	< LOD	0.09	0.02	0.02	0.01	0.01	0.01	0.001

1σ SD: standard deviation.
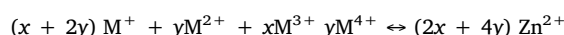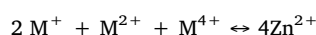LOD: limit of detection.

resolution and low detection limits of analytical instrumentation (Reich et al., 2005; Deditius et al., 2014). Many authors have postulated that Fe in Au-bearing pyrite is mainly derived from siliceous carbonate wall-rocks either by sulfidization or decarbonization processes during fluid/rock interaction, while S in pyrite and other associated trace metals (such as Au, As, Cu) are mainly derived from the hydrothermal fluids (Kesler et al., 2003; Deditius et al., 2014).

In this study, Au is detectable in the three mineralizing stages of pyrite with average concentrations of (0.11 ppm, 0.46 ppm, and 0.17 ppm) for Py-I, Py-II, and Py-III, respectively. The distribution of pyrite in the Qilinchang deposit displays a positive relationship between Au and As (Fig. 11a) in both Py-I and Py-II and a significant negative correlation between Au and As is observed in Py-III. This observation is similar to published data for Au-bearing pyrite in the volcanic-hosted massive sulphide deposit from Bukit Botol, Peninsular Malaysia (Basori et al., 2018). However, the As contents of all pyrite generations (0.096–0.372 wt%) are comparable to As contents of arsenian pyrite (0.23 ppm up to 3.31 wt%) from massive sulphide deposits of the Bathurst Mining Camp, Canada (Soltani Dehnavi et al., 2018). The negative relationship between Au and As in the late-stage pyrite shows that Au is mainly present as inclusions of native gold. However, most of these inclusions may have been formed during the conversion of Au-bearing arsenian pyrite to Au-depleted arsenian pyrite and native gold during diagenesis (Cook et al., 2009). Binary plots between Au and other elements display similar and overlapping trends for Py-II and Py-III. Positive correlations exist between Au versus Ag, Cu, and Sb for Py-II and Py-III relative to Py-I (Fig. 11b, c, d). Meanwhile, in Py-III, there also exists a positive dip correlation of Au versus Bi and Au versus Co (Fig. 11e, f), which may indicate that there are Au-Bi and Au-Co inclusions present in Py-III, in contrast to these elements being within the pyrite structure for Py-I and Py-II.
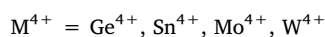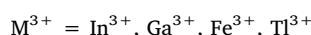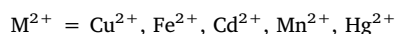
5.2.3. Controls on trace element concentrations of sphalerite

The sphalerite samples display compositional zoning, which occurs in distinct crystallographic planes. The two types of sphalerite based on the paragenetic sequence are classified as early dark-brown (Sph-I) and the late light-yellow sphalerite (Sph-II). These minerals are widely distributed throughout the massive ores and breccia-type ores. Data obtained by LA-ICP-MS summarized in Table 2, highlights the variations in composition and distributions of trace elements in the two generations of sphalerite. In particular, an enrichment of Fe + Cd and other elements are observed in the stage-I sphalerite. The

physicochemical state at the time of primary precipitation, source of ore-forming fluids, and element partitioning between co-existing sulphides and sphalerite are related to the trace element chemistry and its responsible for the incorporation of these elements into the sphalerite structure which explains the substitution mechanisms to be discussed later. The LA-ICP-MS time-resolved depth profiles for these two sphalerite types are relatively flat, but it shows more enrichment of Mn, Fe, Co, Ni, Cu, Ga, Ge, As, Cd, In, Sb, Hg, and Pb in Sph-I comparative to Sph-II. These elements are homogeneously distributed throughout the samples analyzed. The incorporation of these elements into the sphalerite structure occurs via the simple substitution equation as stipulated by Johan (1988), who proposed a general equation to interpret substitution mechanisms for monovalent, bivalent, trivalent, and tetravalent elements in sphalerite:**

$$2\,M^+ + M^{2+} + M^{4+} \leftrightarrow 4Zn^{2+}$$

$$(x + 2y)\,M^+ + y M^{2+} + x M^{3+}\ y M^{4+} \leftrightarrow (2x + 4y)\,Zn^{2+}$$

where $M^+ = Ag^+, Cu^+$

$M^{2+} = Cu^{2+}, Fe^{2+}, Cd^{2+}, Mn^{2+}, Hg^{2+}$

$M^{3+} = In^{3+}, Ga^{3+}, Fe^{3+}, Tl^{3+}$

$M^{4+} = Ge^{4+}, Sn^{4+}, Mo^{4+}, W^{4+}$

(x and y are atomic proportions of M^{3+} and M^{4+}, substituting for Zn^{2+} respectively).

5.2.4. Substitution mechanisms of Zn by other trace elements

The incorporation of trace elements into the sphalerite structure, as explained above by the simple substitution equation of Johan (1988). Previous studies have utilized the LA-ICP-MS data to propose different substitution equations for trace elements in sphalerite (Cook et al., 2009, 2011, 2012; Belissont et al., 2014; Bonnet et al., 2017; Leng et al., 2019). The data generated from our study supported the coupled substitution for $2Zn^{2+} \leftrightarrow Cu^+ + In^{3+}$ because Cu and In do not often occur in a divalent state in sulphides and sulphosalts (Fig. 12a). This same principle applies to the coupled substitution of Ag and Sn replacing Zn as expressed by this equation; $2Zn^{2+} \leftrightarrow Ag^+ + Sn^{3+}$ for Sn substitution in the sphalerite lattice (Fig. 12b). Also, Ag has been found to exist as microscopic Ag-bearing mineral inclusions in sphalerite (Cook et al., 2009; Ciobanu et al., 2011), this exhibit direct substitution in the sphalerite lattice. A positive correlation exists between Ag and Sb
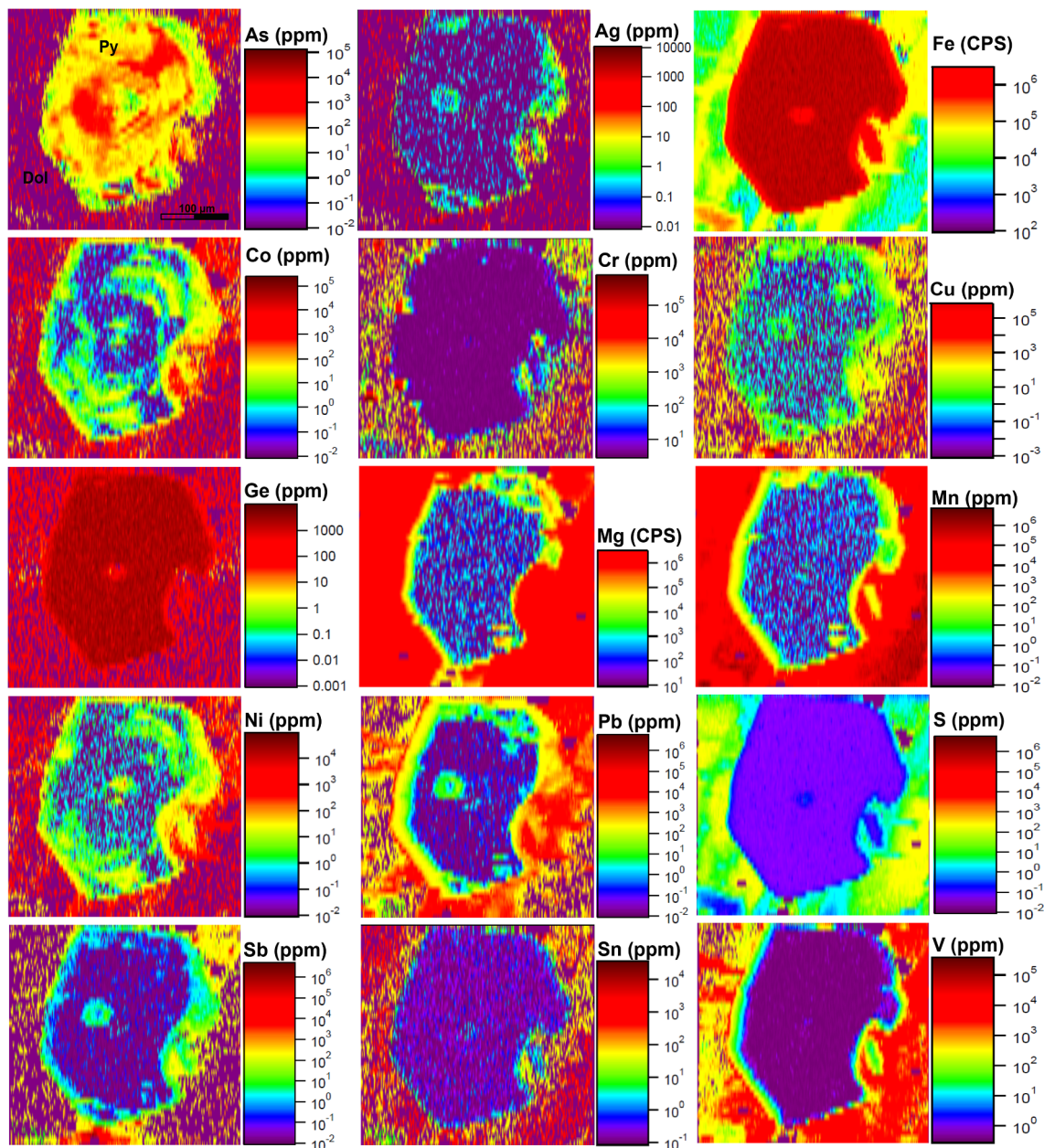
Fig. 8. LA-ICP-MS element maps (As, Ag, Fe, Co, Cr, Cu, Ge, Mg, Mn, Ni, Pb, S, Sb, Sn, V) of Py-I.

(Fig. 12c), as expressed by this substitution equation $2Zn^{2+} \leftrightarrow Ag^+ + Sb^{3+}$. Cook et al. (2009) described similar coupled substitution in sphalerite for the case of this deposit and maybe rightly expressed as $2Zn^{2+} \leftrightarrow Ga^{3+} + (Ag, Cu)^+$ (Fig. 12d). However, Ye et al. (2011) also described similar substitution equations with $3Zn^{2+} \leftrightarrow 2Cu^+ + Sn^{4+}$ (Fig. 12e). Fig. 12f indicates that there is a positively expressed non-correlation between (Cu + Ag) and (In + Sn), of which the valences is expected to produce correlations with monovalent cations for charge balancing (Murakami and Ishihara, 2013), expressed as follows: $3Zn^{2+} \leftrightarrow In^{3+} + Sn^{2+} + (Cu, Ag)^+$ or $4Zn^{2+} \leftrightarrow In^{3+} + Sn^{4+} + (Cu, Ag)^+ + \square$ (where $\square$ denote a vacancy). This involvement of the monovalent cations makes it difficult to distinguish due to the higher concentrations of Cu and Ag compared to In and Sn in most of the spots analyzed.

Accordingly, the positive correlation between In and Sn (Fig. 12g) suggests a potentially coupled substitution $3Zn^{2+} \leftrightarrow In^{3+} + Sn^{3+} + \square$, which is comparable to previous findings (Belissont et al., 2014). The variable oxidation state of Sn poses a problem, its

main oxidation states are Sn^{2+} and Sn^{4+}, but Sn^{3+} constitutes the ample solution to combine with In^{3+} in most samples at a ratio of 1:1 correlation (Epple et al., 2000). However, in Fig. 12h, there exists a steep positive correlation between Cu and Ga + Ge for the two sphalerite types. Dual substitution equations can be inferred from this expression as follows: $2Cu^+ + Ge^{4+} \leftrightarrow 3Zn^{2+}$ and $Cu^+ + Ga^{3+} \leftrightarrow 2Zn^{2+}$. These two equations are in tandem with data reported in previous studies (Cook et al., 2009; Ye et al., 2011; Belissont et al., 2014). These expressions suggest that the two reactions may occur together in both sphalerite types. However, this substitution mechanism of Zn^{2+} by Ge^{2+} could be suggestive of a reducing condition in the ore-forming fluids.

5.3. Source of ore metals

The origin of ore metals of Zn and Pb can be determined from the source of pyrite with the assumption that the elements of Zn, Pb, and Fe have a conventional source. The Co and Ni abundances in sedimentary
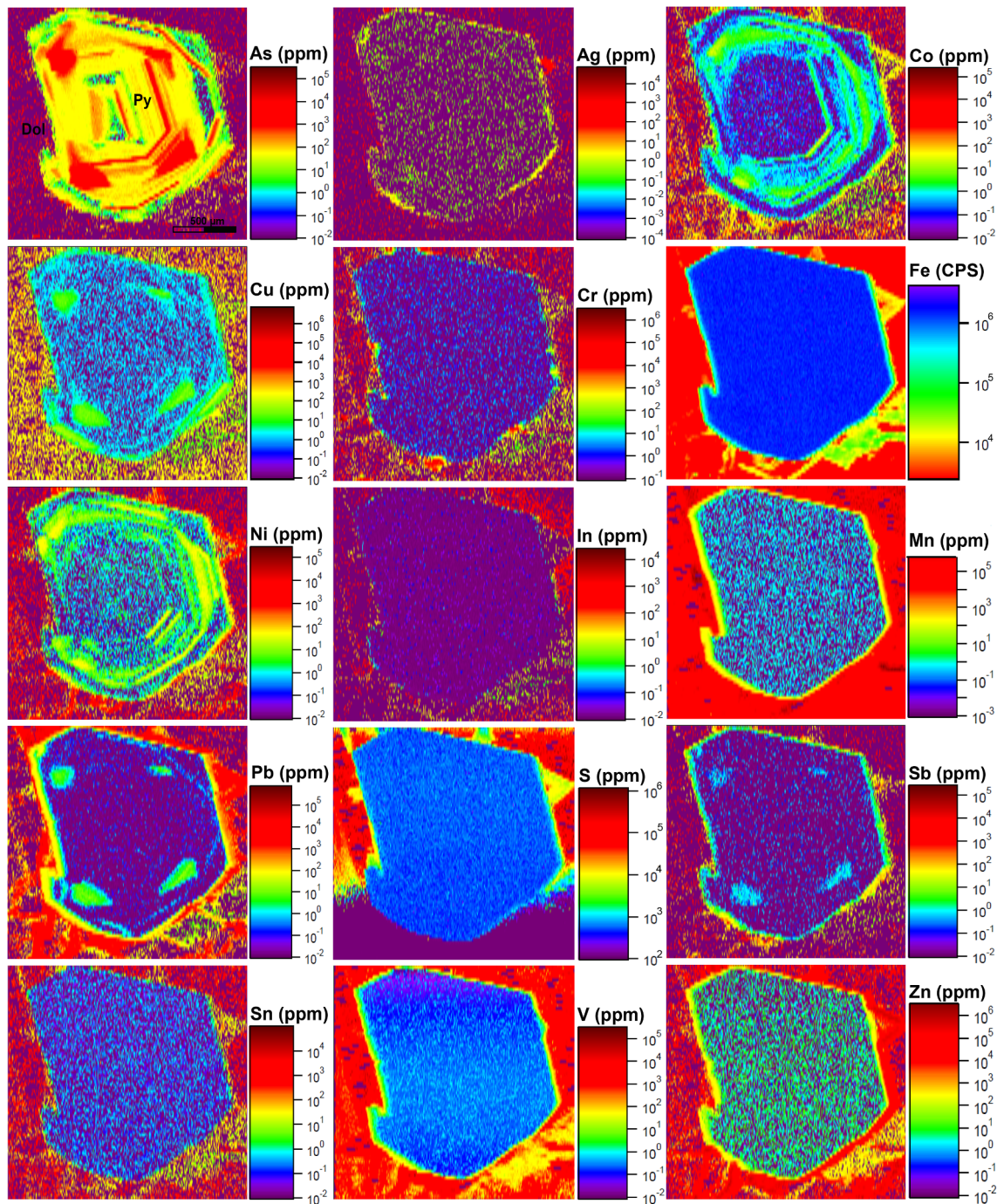
Fig. 9. LA-ICP-MS element maps (As, Ag, Co, Cu, Cr, Fe, Ni, In, Mn, Pb, S, Sb, Sn, V, Zn) of Py-III surrounded by a groundmass of dolomite.

sulphides are controlled by many variables such as; ΣCo, ΣNi, ΣFe, pH, Eh, and organic content. Usually, the Co/Ni ratios in sedimentary pyrite are generally between 0.01 and 10 (Gregory et al., 2015) compared to hydrothermal and massive sulphide deposits with Co/Ni ratios of 1.17 and 8.70, respectively. Cobalt and Ni, which often display similar geochemistry and can be easily incorporated into the crystal lattice of pyrite and is not readily discharged during recrystallization (Tribovillard et al., 2006; Large et al., 2009; Koglin et al., 2010). The Co/Ni ratio of pyrite is advantageous in discriminating pyrite with different origins (Price, 1972; Bralia et al., 1979). Pyrite with high Co and Ni concentrations may originate from the high-temperature, magmatic-hydrothermal regime and is related to mafic sources, particularly where Co/Ni ratios are higher than zero in contrast to sedimentary

environments where pyrite exhibits low Co/Ni ratios. Previous studies have shown that high Co/Ni ratios occur in pyrite from volcanogenic ores (~Co/Ni > 10), whereas lower temperature hydrothermal pyrite generally has Co/Ni ratios between ~5 and 10 (Bralia et al., 1979). A compilation of Co/Ni ratios by Bajwah et al. (1987) shows that pyrite from magmatic-hydrothermal deposits has Co/Ni ratios between ~1 and 10, whereas pyrite from orthomagmatic segregation deposits displays high but variable Co and Ni contents (up to wt.% levels), and generally Co/Ni ratios of < 1. The Co/Ni ratios of pyrite from the Qilinchang deposit are compared with those of pyrite from sedimentary exhalative (SEDEX) and MVT deposits (Fig. 13a), volcanic-hosted massive sulphide (VHMS) deposits (Fig. 13b), iron oxide copper-gold (IOCG) deposits (Fig. 13c), porphyry Cu deposits (Fig. 13d),
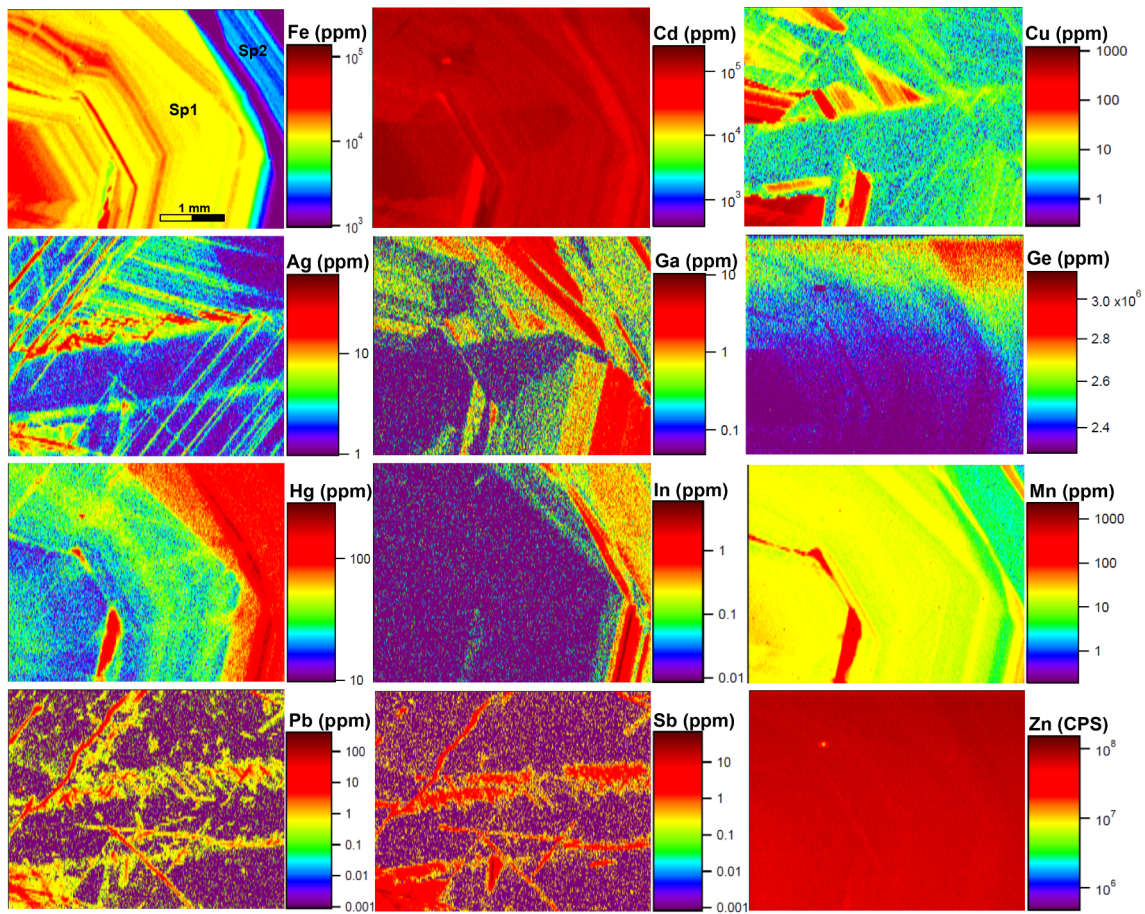
Fig. 10. LA-ICP-MS element maps (Fe, Cd, Cu, Ag, Ga, Ge, Hg, In, Mn, Pb, Sb, Zn) in dark and light bands of sphalerite.
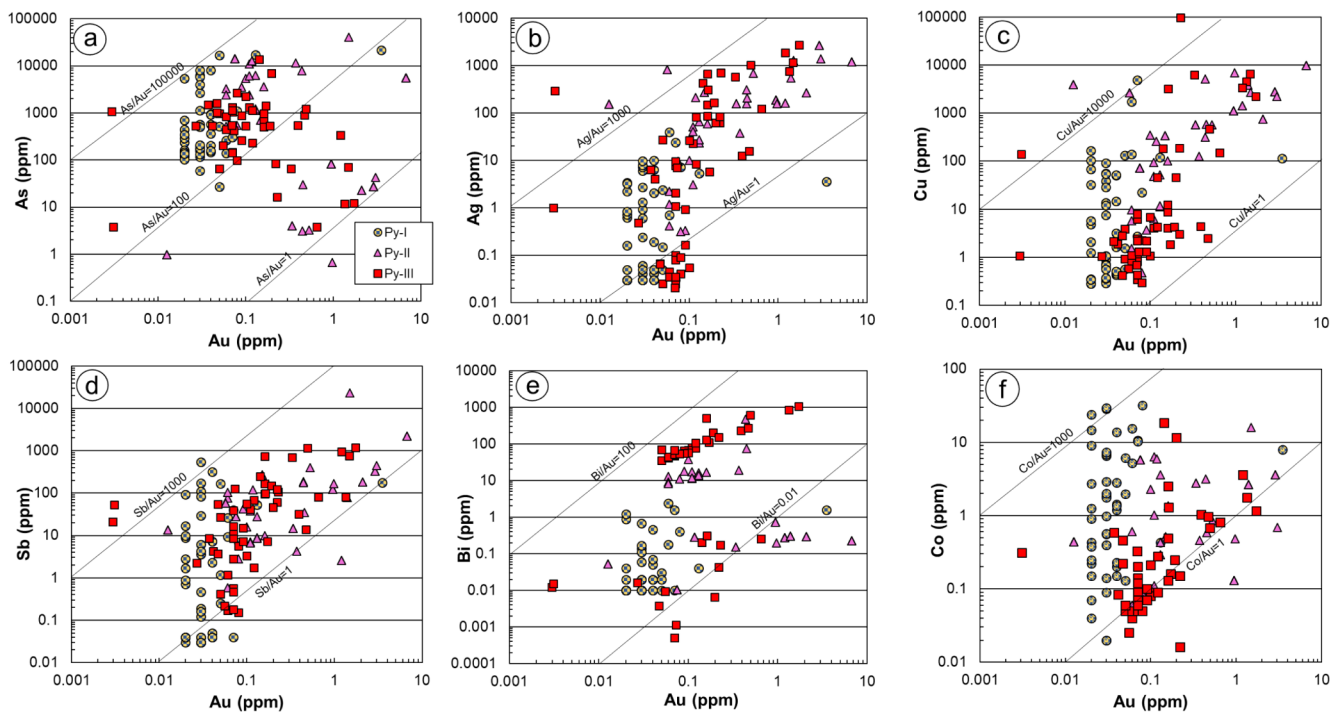

Fig. 11. Binary plots of selected trace elements versus Au in Py-I, Py-II and Py-III (a) As *vs.* Au, (b) Ag *vs.* Au, (c) Cu *vs.* Au, (d) Sb *vs.* Au, (e) Bi *vs.* Au, and (f) Co *vs.* Au from the Qilinchang deposit.
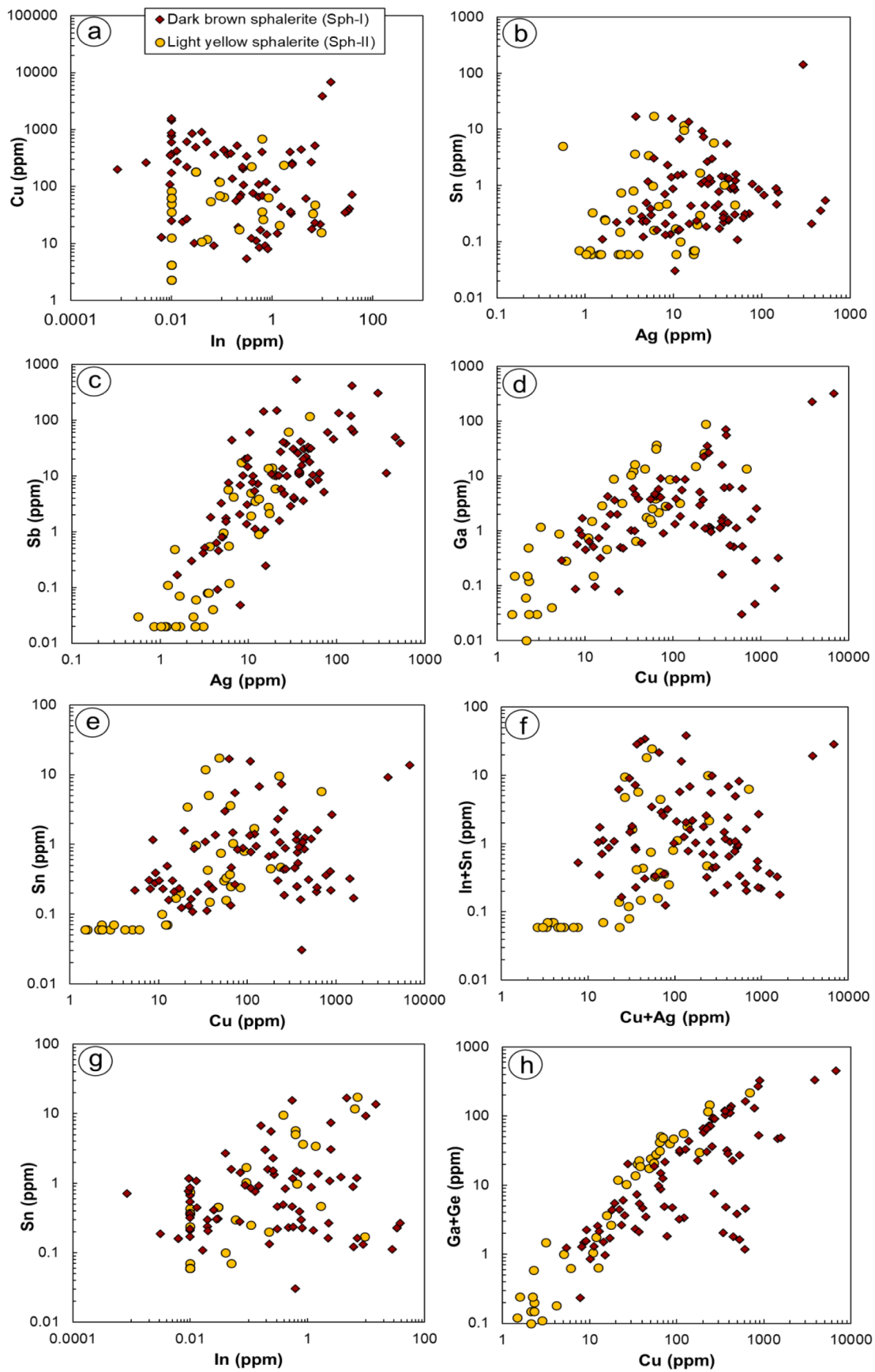
Fig. 12. Binary plots of (a) Cu *vs.* In, (b) Sn *vs.* Ag, (c) Sb *vs.* Ag, (d) Ga *vs.* Cu, (e) Sn *vs.* Cu, (f) (In + Sn) *vs.* (Cu + Ag), (g) Sn *vs.* In, and (h) (Ga + Ge) *vs.* Cu from the Qilinchang deposit.
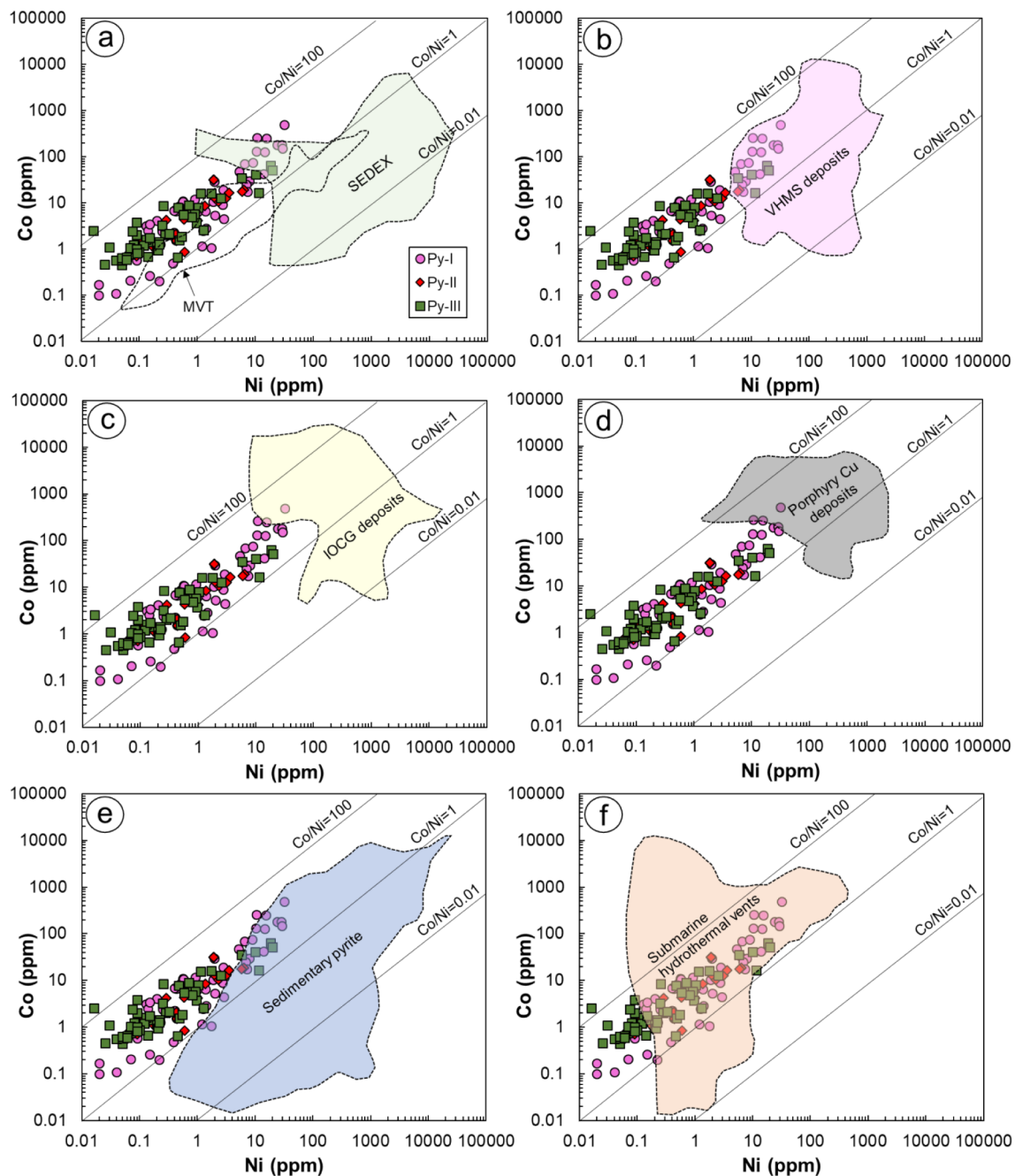
Fig. 13. Binary plots of Co *vs.* Ni contents in pyrite from Qilinchang Pb-Zn deposit. Geochemical data for pyrite from other deposits are displayed as coloured fields, except for pyrite from MVT Pb-Zn deposits as a dash line polygon. (a) SEDEX (Howard's Pass district of Canada, McArthur Basin of Australia) (Gadd et al., 2016; Mukherjee and Large, 2017) and MVT deposits (Jinding and Hoshbulak, China) (Li et al., 2015; Wang et al., 2018). (b) VHMS deposits (Keketale in Altay of NW China, Bathurst and Matagami districts of Canada, Pontide of NE Turkey) (Zheng et al., 2013; Revan et al., 2014; Genna and Gaboury, 2015; Soltani Dehnavi et al., 2015). (c) IOCG deposits (Ernest Henry of Australia and Manto Verde of Chile) (Rieger et al., 2010; Rusk et al., 2010). (d) Porphyry Cu deposits (Dexing and Jinchang of China, Metaliferi Mountains of Romania) (Reich et al., 2013; Cioacă et al., 2014; Zhang et al., 2016). (e) Sedimentary pyrite (Global) (Berner et al., 2013; Large et al., 2014; Gregory et al., 2017; Mukherjee and Large, 2017). (f) Submarine hydrothermal vents (Keith et al., 2016).

sedimentary pyrite (Fig. 13e), and submarine hydrothermal vents deposits (Fig. 13f). Py-I display higher contents of Co and Ni with Co/Ni ratio ranging from 0.04 to 1.6. Py-II and Py-III have identical but varied content of Co and Ni with Co/Ni ratios ranging from 0 to 0.706 and 0–0.696, respectively. Conclusively, the pyrite from the Qilinchang deposit has Co/Ni ratios slightly lower but comparable to typical MVT deposits (0.2–7.2) and completely different from IOCG deposits and porphyry Cu deposits. The Co and Ni contents in the Qilinchang pyrite are lower compared to those of IOCG and porphyry Cu deposits, suggesting the lack of magmatic activities and absence of a genetic

relationship between the Pb-Zn mineralization and Permian Emeishan basalts.

5.4. Significance of trace element trends in pyrite and sphalerite

Principal component analysis is critical to the study of multivariate data. It is one of the oldest statistical multivariate techniques, and more recently, it has progressed to be the subject of various research, ranging from new-model based methods to algorithmic illustrations from neural networks. PCA as a machine learning tool is similar to clustering, and it
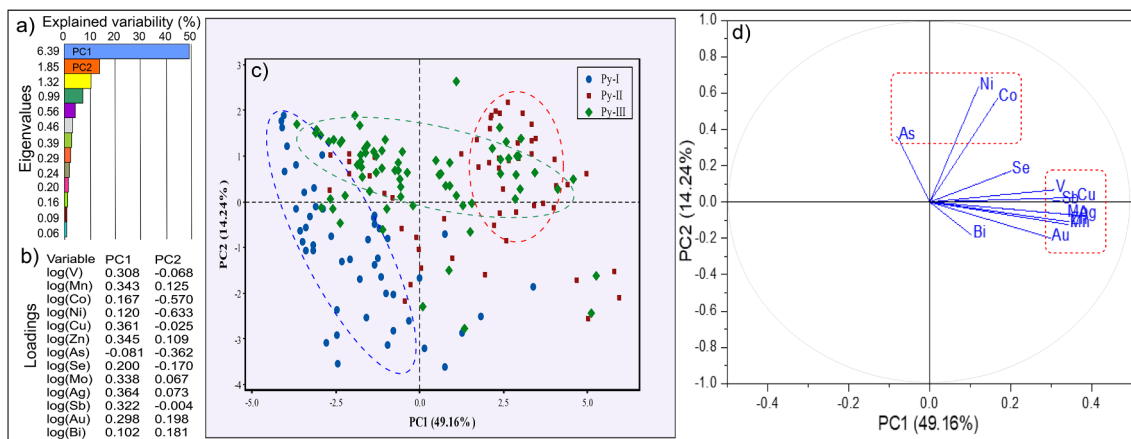
Fig. 14. Principal component analysis of the LA-ICP-MS log-transformed dataset of trace element contents in pyrite from Qilinchang {175 spot analysis (individuals), 13 elements (variables)}. On the left-hand corner: eigenvalues (a) (i.e., explained variability) and loadings (b) (i.e., eigenvector coefficients) of the principal components. Middle image: spot analyses (c) (i.e., individuals) plotted on the PC1 *vs.* PC2 plane (explaining 63.4% of element content variability). Right-hand image: elements (d) (i.e., variables) plotted in the same plane. This PCA underlines two mains, opposed clusters of elements distributed among the pyrite types: a cluster of elements showing similar behaviour are marked as (As, Ni, Co) and (Ag, Bi, Cu, Sb, Se, Zn, Mn, Mo, Au, V).

integrates the complexity in the multi-dimensional dataset while retaining trends and patterns (Frenzel et al., 2016). Hence, PCA has been applied in this study to provide information on the underlying ore mineralization and the distribution trends of elements in the mineralizing stages. The elements and spot analyses of the minerals in each sample from the different paragenetic stages discriminate the element compositions of each ore stage using large datasets.

Meanwhile, the elements and spots analyses of pyrite occurrence in the paragenetic sequence are projected on the PC1 *vs.* PC2 plane, which accounts for 63.4% of element content variability (Fig. 14). Two loading factors were used for this interpretation with factor one primarily loaded by V, Mn, Cu, Zn, Se, Mo, Ag, Sb, Au, and Bi, while factor two is mainly loaded by Co, Ni, and As. Describing the evolution and variational trends of the ore-forming fluids in the Qilinchang deposit, the fluid was enriched in Co, Ni, and As and partitioned into another fluid subsequently enriched in V, Mn, Cu, Zn, Se, Mo, Ag, Sb, Au, and Bi. The low Ni, Co, and In contents in the pyrite typically suggests that the ore-forming fluids are not related to magmatic contributions. The variation in temporal and broad evolution of pyrite gives assumptions to trace element availability and changes in physical and chemical conditions at the period of pyrite formation. Py-I is discerned from

other pyrite types due to its higher Mg, Mn, Co, Ni, and Tl contents. This suggests that ore-forming fluids were initially rich in these metals during the early Py-Sph stage. The contents of Co and Ni decreased from Py-I to Py-III because of constant pyrite precipitation during fluid evolution, and these elements are mainly partitioned or substituted into the lattice of pyrite even though co-existing with sphalerite. Py-II is differentiated from other pyrite types by elevated contents of Cu, As, Se, Mo, and Sb. The higher concentrations of Cu and As in Py-II denote the relative enrichment of these elements in the ore-forming fluids due to evolving fluids and lack of chalcopyrite in the Sph-Gn-Py stage. Py-III can also be discriminated from Py-I and Py-II due to higher contents of Ag-Pb mineral phases. Owing to the presence of galena in this stage, Ag, Pb, and Bi partition into the pyrite lattice as inclusions of Ag-bearing minerals. Also, higher contents of Ti, V, and Cr in Py-III may imply enhanced carbonate replacement in this stage since these elements are mainly partitioned into carbonate inclusions in pyrite. This is observed by extensive replacement relic textures of Py-III by carbonate minerals.

Similarly, the elements and spot analyses of sphalerite in the mineralizing fluids presented as PC1 *vs.* PC2 (Fig. 15) accounted for 60.57% of element explained variability. Two loading factors were also considered for the projection of the PCs, of which factor one mainly
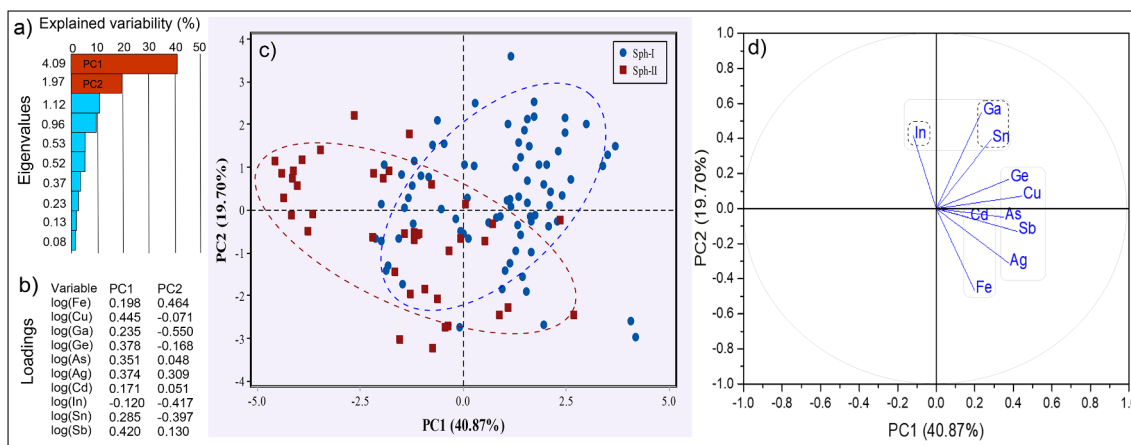

Fig. 15. Principal component analysis of the LA-ICP-MS log-transformed dataset of trace element contents in sphalerite from Qilinchang {119 spot analysis (individuals), 10 elements (variables)}. On the left-hand corner: eigenvalues (a) (i.e., explained variability) and loadings (b) (i.e., eigenvector coefficients) of the principal components. Middle image: spot analyses (c) (i.e., individuals) plotted on the PC1 *vs.* PC2 plane (explaining 60.57% of element content variability). Right-hand image: elements (d) (i.e., variables) plotted in the same plane. This PCA underlines two mains, opposed clusters of elements distributed among the sphalerite types: a cluster of elements showing similar behaviour are marked as (In, Sn, Ga) and (Ge, Cu, As, Sb, Ag, Cd, Fe).

loaded by Cu, Ge, As, Ag, Sb, Cd, and Fe, while factor two is loaded by Ga, In, and Sn. The initial fluid enriched in elements loaded in factor one evolved into another fluid with elevated concentrations of Ga, In, and Sn. The enrichment of Ge, Ga, and As in partitioned fluids is an indication of low-temperature deposit. The evolution trends of the hydrothermal fluids evidenced from S, C, O, and Pb isotopic studies earlier carried out in the study area (Zhou et al., 2001; Han et al., 2007; Zhang et al., 2009; Zhang et al., 2017; Xu et al., 2019) suggests a process of fluid mixing, which is typically common in a low-temperature environment. The C and O isotopic characteristics suggest that the ore-forming fluids were mainly derived from water-rock interaction between the mantle/metamorphic fluids and carbonates (Zhang et al., 2009; Zhang et al. 2017). The δ^{34}S of sulphides is related to the thermochemical sulfate reduction (TSR) of Carboniferous seawater sulfate and are mainly derived from evaporites in the host strata producing H_2S-rich fluid by TSR with restricted inducement from mantle-derived sulphur (Meng et al., 2019). Also, the homogenous composition of Pb isotopic data of galena (Bao et al., 2017) indicates that the metals were predominantly originated from the clastic rocks of the Mesoproterozoic-early Neoproterozoic rocks of the Kunyang Group and Cambrian to Permian strata. It is assumed that the wide ranges of trace elements were attributed to the ore-forming fluids migrating upward along the deeply buried faults, mixing with evaporites present within the basement and carbonate strata, extracting Pb, Zn, S, and other metallic elements to form the economic deposit.

6. Conclusions

LA-ICP-MS analyses have been used to investigate the concentrations, source, and elemental substitution mechanisms in different generations of pyrite and sphalerite in the Qilinchang Pb-Zn deposit. Our main findings are summarized as follows:

(1) The observed variations in the pyrite reveal varied substitution mechanisms responsible for the evolution of the pyrite. Py-I is enriched in Mg, Mn, Co, Ni, and Tl compared to Py-II and Py-III, while Py-II is more concentrated in Cu, As, Se, Mo, Ag, and Sb. Py-III have variable concentrations of trace elements and also have higher inclusions of Ag-Pb-mineral bearing phases.

(2) Sphalerite trace element compositions display higher values of Mn, Fe, Co, Ni, Cu, Ga, Ge, As, Ag, Cd, Sb, Hg, and Pb in the early stage type-I compared to the type-II. The physicochemical condition at the time of initial precipitation, source of ore-forming fluids and element partitioning between associated sulphides and sphalerite are main factors responsible for the incorporation of these elements, which is primarily through simple substitution mechanisms (e.g., $2Zn^{2+} \leftrightarrow Cu^+ + In^{3+}$) as indicated from binary plots and PCA.

(3) Taking into account the low Co/Ni ratios of pyrite and evolution trends of the ore-forming fluids, we suggest that the Qilinchang deposit was not related to magmatic activities and hence, deposited in a low-temperature environment which is analogous to typical MVT deposits.

7. Authors agreement

All the authors contributed equally to the preparation of this manuscript. All authors read and approved the final manuscript.

Author contributions

Abiola Oyebamiji: Conceptualization, Data acquisition, Investigation, Methodology, Software, Writing - original draft, Writing - review & editing. **Ruizhong Hu:** Funding acquisition, Project administration, Supervision, Resources, Writing - review & editing. **Chenghai Zhao:** Methodology, Visualization, Writing - original draft. **Tehseen Zafar:** Visualization, Writing - original draft, Writing - review & editing.

Declaration of Competing Interest

The authors declare that they have no known competing financial interests or personal relationships that could have appeared to influence the work reported in this paper.

Acknowledgments

Appendix A. Supplementary material

Supplementary data to this article can be found online at https://doi.org/10.1016/j.jseaes.2020.104292.

References

Abraitis, P., Pattrick, R., Vaughan, D., 2004. Variations in the compositional, textural and electrical properties of natural pyrite: a review. Int. J. Miner. Process. 74, 41–59.

Bajwah, Z.U., Seccombe, P.K., Offler, R., 1987. Trace element distribution Co: Ni ratios and genesis of the Big Cadia iron-copper deposit, New South Wales, Australia. Miner. Deposita 22, 292–300.

Bao, Z., Li, Q., Wang, C.Y., 2017. Metal source of giant Huize Zn-Pb deposit in SW China: new constraints from in situ Pb isotopic compositions of galena. Ore Geol. Rev. 91, 824–836.

Barker, S.L., Hickey, K.A., Cline, J.S., Dipple, G.M., Kilburn, M.R., Vaughan, J.R., Longo, A.A., 2009. Uncloaking invisible gold: use of nanoSIMS to evaluate gold, trace elements, and sulfur isotopes in pyrite from Carlin-type gold deposits. Econ. Geol. 104, 897–904.

Basori, M.B.I., Gilbert, S., Large, R.R., Zaw, K., 2018. Textures and trace element composition of pyrite from the Bukit Botol volcanic-hosted massive sulphide deposit, Peninsular Malaysia. J. Asian Earth Sci. 158, 173–185.

Belissont, R., Boiron, M.C., Luais, B., Cathelineau, M., 2014. LA-ICP-MS analyses of minor and trace elements and bulk Ge isotopes in zoned Ge-rich sphalerites from the Noailhac–Saint-Salvy deposit (France): insights into incorporation mechanisms and ore deposition processes. Geochim. Cosmochim. Acta 126, 518–540.

Berner, Z.A., Puchelt, H., NÖltner, T., Kramar, U.T.Z., 2013. Pyrite geochemistry in the Toarcian Posidonia Shale of south-west Germany: evidence for contrasting trace-element patterns of diagenetic and syngenetic pyrites. Sedimentology 60, 548–573.

Bonnet, J., Mosser-Ruck, R., Caumon, M.C., Rouer, O., Andre-Mayer, A.S., Cauzid, J., Peiffert, C., 2016. Trace element distribution (Cu, Ga, Ge, Cd, and Fe) IN sphalerite from the tennessee MVT deposits, USA, by combined EMPA, LA-ICP-MS, Raman spectroscopy, and crystallography. Can. Miner. 54, 1261–1284.

Bonnet, J., Cauzid, J., Testemale, D., Kieffer, I., Proux, O., Lecomte, A., Bailly, L., 2017. Characterization of germanium speciation in sphalerite (ZnS) from Central and Eastern Tennessee, USA, by X-ray absorption spectroscopy. Minerals 7, 1–16.

Bralia, A., Sabatini, G., Troja, F., 1979. A revaluation of the Co/Ni ratio in pyrite as geochemical tool in ore genesis problems. Miner. Deposita 14, 353–374.

Cioacă, M.E., Munteanu, M., Qi, L., Costin, G., 2014. Trace element concentrations in porphyry copper deposits from Metaliferi Mountains, Romania: a reconnaissance study. Ore Geol. Rev. 63, 22–39.

Ciobanu, C.L., Cook, N.J., Utsunomiya, S., Pring, A., Green, L., 2011. Focussed ion beam–transmission electron microscopy applications in ore mineralogy: bridging micro-and nanoscale observations. Ore Geol. Rev. 42, 6–31.

Ciobanu, C.L., Cook, N.J., Utsunomiya, S., Kogawa, M., Green, L., Gilbert, S., Wade, B., 2012. Gold-telluride nanoparticles revealed in arsenic-free pyrite. Am. Mineral. 97, 1515–1518.

Cook, N.J., Ciobanu, C.L., Pring, A., Skinner, W., Shimizu, M., Danyushevsky, L., Saini-Eidukat, B., Melcher, F., 2009. Trace and minor elements in sphalerite: A LA-ICPMS study. Geochim. Cosmochim. Acta 73, 4761–4791.

Cook, N.J., Sundblad, K., Valkama, M., Nygård, R., Ciobanu, C.L., Danyushevsky, L., 2011. Indium mineralisation in A-type granites in southeastern Finland: insights into mineralogy and partitioning between coexisting minerals. Chem. Geol. 284, 62–73.

Cook, N.J., Ciobanu, C.L., Brugger, J., Etschmann, B., Howard, D.L., de Jonge, M.D., Ryan, C., Paterson, D., 2012. Determination of the oxidation state of Cu in substituted Cu-In-Fe-bearing sphalerite via μ-XANES spectroscopy. Am. Mineral. 97, 476–479.

Cook, N.J., Ciobanu, C.L., Meria, D., Silcock, D., Wade, B., 2013. Arsenopyrite-pyrite association in an orogenic gold ore: tracing mineralization history from textures and trace elements. Econ. Geol. 108, 1273–1283.

Cook, N.J., Ciobanu, C.L., George, L., Zhu, Z.Y., Wade, B., Ehrig, K., 2016. Trace element

analysis of minerals in magmatic-hydrothermal ores by laser ablation inductively-coupled plasma mass spectrometry: approaches and opportunities. Minerals 6, 1–34.

Deditius, A.P., Utsunomiya, S., Ewing, R.C., Kesler, S.E., 2009a. Nanoscale "liquid" in-clusions of As-Fe-S in arsenian pyrite. Am. Mineral. 94, 391–394.

Deditius, A.P., Utsunomiya, S., Ewing, R.C., Chryssoulis, S.L., Venter, D., Kesler, S.E., 2009b. Decoupled geochemical behavior of As and Cu in hydrothermal systems. Geology 37, 707–710.

Deditius, A.P., Utsunomiya, S., Reich, M., Kesler, S.E., Ewing, R.C., Hough, R., Walshe, J., 2011. Trace metal nanoparticles in pyrite. Ore Geol. Rev. 42, 32–46.

Deditius, A.P., Reich, M., Kesler, S.E., Utsunomiya, S., Chryssoulis, S.L., Walshe, J., Ewing, R.C., 2014. The coupled geochemistry of Au and As in pyrite from hydro-thermal ore deposits. Geochim. Cosmochim. Acta 140, 644–670.

Epple, M., Panthöfer, M., Walther, R., Deiseroth, H.J., 2000. Crystal-chemical char-acterization of mixed valence indium chalcogenides by X-ray absorption spectroscopy (EXAFS). Z. Kristallogr. 215, 445–453.

Fan, Y., Zhou, T., Yuan, F., Wu, M., 2014. Geological and geochemical constraints on the genesis of the Xiangquan Tl-only deposit, eastern China. Ore Geol. Rev. 59, 97–108.

Frenzel, M., Hirsch, T., Gutzmer, J., 2016. Gallium, germanium, indium, and other trace and minor elements in sphalerite as a function of deposit type-A meta-analysis. Ore Geol. Rev. 76, 52–78.

Gadd, M.G., Layton-Matthews, D., Peter, J.M., Paradis, S.J., 2016. The world-class Howard's Pass SEDEX Zn-Pb district, Selwyn Basin, Yukon. Part I: trace element compositions of pyrite record input of hydrothermal, diagenetic, and metamorphic fluids to mineralization. Miner. Deposita 51, 319–342.

Genna, D., Gaboury, D., 2015. Deciphering the hydrothermal evolution of a VMS system by LA-ICP-MS using trace elements in pyrite: an example from the Bracemac-McLeod deposits, Abitibi, Canada, and implications for exploration. Econ. Geol. 110, 2087–2108.

George, L.L., Cook, N.J., Ciobanu, C.L., 2016. Partitioning of trace elements in co-crys-tallized sphalerite-galena-chalcopyrite hydrothermal ores. Ore Geol. Rev. 77, 97–116.

Gregory, D.D., Large, R.R., Halpin, J.A., Baturina, E.L., Lyons, T.W., Wu, S., Danyushevsky, L., Sack, P.J., Chappaz, A., Maslennikov, V.V., 2015. Trace element content of sedimentary pyrite in black shales. Econ. Geol. 110, 1389–1410.

Gregory, D.D., Lyons, T.W., Large, R.R., Jiang, G., Stepanov, A.S., Diamond, C.W., Figueroa, M.C., Olin, P., 2017. Whole rock and discrete pyrite geochemistry as complementary tracers of ancient ocean chemistry: an example from the Neoproterozoic Doushantuo Formation. China. Geochim. Cosmochim. Acta 216, 201–220.

Han, R.S., Chen, J., Li, Y., Gao, D.R., Ma, D.Y., 2001. Discovery of concealed No.8 ore-body at Qilinchang lead-zinc deposit in Huize mine, Yunnan. Geol. Geochem. 29, 191–195 (in Chinese with English abstract).

Han, R.S., Liu, C.Q., Huang, Z.L., Ma, D.Y., Li, Y., Hu, B., Ma, G.S., Lei, L., 2004. Fluid inclusion of calcite and sources of ore-forming fluids in the Huize Zn-Pb-(Ag-Ge) district, Yunnan, China. Acta Geol. Sinic. (Engl. Ed.) 78, 583–591.

Han, R.S., Chen, J., Huang, Z.L., Ma, D.Y., Xue, C.D., Li, Y., Zou, H.J., Li, B., Hu, Y.Z., 2006. Dynamics of tectonic ore-forming process and localization prognosis of con-cealed ore- bodies- as exemplified by the Huize super-large Zn-Pb-(Ag-Ge) District, Yunnan, vol. 1, 128–158 (in Chinese with English abstract).

Han, R.S., Liu, C.Q., Huang, Z.L., Chen, J., Ma, D.Y., Lei, L., Ma, G.S., 2007. Geological features and origin of the Huize carbonate-hosted Zn-Pb-(Ag) District, Yunnan, South China. Ore Geol. Rev. 31, 360–383.

Han, R.S., Hu, Y.Z., Wang, X.K., Hou, B.H., Huang, Z.L., Chen, J., Wang, F., Wu, P., Li, B., Wang, H.J., Dong, Y., Lei, L., 2012. Mineralization model of rich Ge-Ag-bearing Zn-Pb polymetallic deposit concentrated district in northeastern Yunnan, China. Acta Geol. Sinic. 86, 280–294 (in Chinese with English abstract).

Han, R.S., Li, W., Qiu, W., Ren, T., Wang, F., 2014. Typical geological features of rich Zn-Pb-(Ge-Ag) deposits in Northeastern Yunnan, China. Acta Geol. Sinic. 88, 160–162 (in Chinese with English abstract).

Hu, R.Z., Zhou, M.F., 2012. Multiple Mesozoic mineralization events in South China -an introduction to the thematic issue. Miner. Deposita 47, 579–588.

Huang, Z.L., Chen, J., Han, R.S., Li, W.B., Liu, C.Q., Zhang, Z.L., Ma, D.Y., Gao, D.R., Yang, H.L., 2004. Geochemistry and ore-formation of the huize giant lead-zinc de-posit, Yunnan, province, China: discussion on the relationship between the emeishan flood basalts and lead-zinc mineralization. Geol. Pub. House 1–214 Beijing (in Chinese).

Iwamori, H., Albaréde, F., Nakamura, H., 2010. Global structure of mantle isotopic het-erogeneity and its implications for mantle differentiation and convection. Earth Planet. Sci. Lett. 299, 339–351.

Johan, Z., 1988. Indium and germanium in the structure of sphalerite: an example of coupled substitution with copper. Mineral. Petrol. 39, 211–229.

Keith, M., Häckel, F., Haase, K.M., Schwarz-Schampera, U., Klemd, R., 2016. Trace ele-ment systematics of pyrite from submarine hydrothermal vents. Ore Geol. Rev. 72, 728–745.

Kesler, S.E., Russell, N., McCurdy, K., 2003. Trace-metal content of the Pueblo Viejo precious-metal deposits and their relation to other high-sulfidation epithermal sys-tems. Miner. Deposita 38, 668–682.

Koglin, N., Frimmel, H.E., Minter, W.L., Brätz, H., 2010. Trace-element characteristics of different pyrite types in Mesoarchaean to Palaeoproterozoic placer deposits. Miner. Deposita 45, 259–280.

Lach, P., Mercadier, J., Dubessy, J., Boiron, M.C., Cuney, M., 2013. In situ quantitative measurement of rare earth elements in uranium oxides by laser ablation-inductively coupled plasma-mass spectrometry. Geostand. Geoanal. Res. 37, 277–296.

Large, D.J., Sawłowicz, Z., Spratt, J., 1999. A cobaltite-framboidal pyrite association from the Kupferschiefer: possible implications for trace element behaviour during the earliest stages of diagenesis. Mineral. Mag. 63, 353–361.

Large, R.R., Maslennikov, V.V., Robert, F., Danyushevsky, L.V., Chang, Z., 2007. Multistage sedimentary and metamorphic origin of pyrite and gold in the giant Sukhoi Log deposit, Lena gold province, Russia. Econ. Geol. 102, 1233–1267.

Large, R.R., Danyushevsky, L., Hollit, C., Maslennikov, V., Meffre, S., Gilbert, S., Bull, S., Scott, R., Emsbo, P., Thomas, H., 2009. Gold and trace element zonation in pyrite using a laser imaging technique: implications for the timing of gold in orogenic and Carlin-style sediment-hosted deposits. Econ. Geol. 104, 635–668.

Large, R.R., Meffre, S., Burnett, R., Guy, B., Bull, S., Gilbert, S., Goemann, K., Danyushevsky, L., 2013. Evidence for an intrabasinal source and multiple con-centration processes in the formation of the Carbon Leader Reef, Witwatersrand Supergroup, South Africa. Econ. Geol. 108, 1215–1241.

Large, R.R., Halpin, J.A., Danyushevsky, L.V., Maslennikov, V.V., Bull, S.W., Long, J.A., Gregory, D.D., Lounejeva, E., Lyons, T.W., Sack, P.J., McGoldrick, P.J., 2014. Trace element content of sedimentary pyrite as a new proxy for deep-time ocean-atmo-sphere evolution. Earth Planet. Sci. Lett. 389, 209–220.

Leng, C.B., Wang, W., Ye, L., Zhang, X.C., 2019. Genesis of the late Ordovician Kukaazi Pb-Zn deposit in the western Kunlun orogen, NW China: new insights from in-situ trace elemental compositions of base metal sulfides. J. Asian Earth Sci. 184, 103995.

Li, W.B., Huang, Z.L., Wang, Y.X., Chen, J., Han, R.S., Xu, C., Yin, M.D., 2004. Age of the giant Huize Zn-Pb deposits determined by Sm-Nd dating of hydrothermal calcite. Geol. Rev. 50, 189–195.

Li, X.B., Huang, Z.L., Li, W.B., Zhang, Z.L., Yan, Z.F., 2006. Sulfur isotopic compositions of the Huize super-large Pb-Zn deposit, Yunnan Province, China: implications for the source of sulfur in the ore-forming fluids. J. Geochem. Explor. 89, 227–230.

Li, W.B., Huang, Z.L., Yin, M.D., 2007. Dating of the giant Huize Zn-Pb ore field of Yunnan province, southwest China: constraints from the Sm-Nd system in hydro-thermal calcite. Resour. Geol. 57, 90–97.

Li, Z., Xue, C., Wu, Y., Dong, X., Wang, S., Chen, J., 2015. The nappe-hosted Hoshbulak MVT Zn-Pb deposit, Xinjiang, China: a review of the geological, elemental and stable isotopic constraints. Ore Geol. Rev. 70, 47–60.

Liu, H.C., Lin, W.D., 1999. Study on the Law of Pb-Zn-Ag Ore Deposit in Northeast Yunnan. Yunnan University Press, Kunming, China, pp. 1–468 (in Chinese).

Lockington, J.A., Cook, N.J., Ciobanu, C.L., 2014. Trace and minor elements in sphalerite from metamorphosed sulfide deposits. Mineral. Petrol. 108, 873–890.

Meng, Y.M., Hu, R.Z., Huang, X.W., Gao, J.F., Sasseville, C., 2019. The origin of the carbonate-hosted Huize Zn-Pb-Ag deposit, Yunnan province, SW China: constraints from the trace element and sulfur isotopic compositions of pyrite. Mineral. Petrol. 113, 369–391.

Mukherjee, I., Large, R., 2017. Application of pyrite trace element chemistry to ex-ploration for SEDEX style Zn-Pb deposits: McArthur Basin, Northern Territory, Australia. Ore Geol. Rev. 81, 1249–1270.

Murakami, H., Ishihara, S., 2013. Trace elements of Indium-bearing sphalerite from tin-polymetallic deposits in Bolivia, China and Japan: a femto-second LA-ICPMS study. Ore Geol. Rev. 53, 223–243.

Pfaff, K., Koenig, A., Wenzel, T., Ridley, I., Hildebrandt, L.H., Leach, D.L., Markl, G., 2011. Trace and minor element variations and sulfur isotopes in crystalline and colloform ZnS: incorporation mechanisms and implications for their genesis. Chem. Geol. 286, 118–134.

Price, B.J., 1972. Minor Elements in Pyrites from the Smithers Map Area, B.C. and Exploration Applications of Minor Element Studies. Unpublished M.S. thesis. University of British, Columbia, Vancouver, Canada, pp. 1–291.

Reich, M., Kesler, S.E., Utsunomiya, S., Palenik, C.S., Chryssoulis, S.L., Ewing, R.C., 2005. Solubility of gold in arsenian pyrite. Geochim. Cosmochim. Acta 69, 2781–2796.

Reich, M., Utsunomiya, S., Kesler, S.E., Wang, L., Ewing, R.C., Becker, U., 2006. Thermal behavior of metal nanoparticles in geologic materials. Geology 34, 1033–1036.

Reich, M., Deditius, A., Chryssoulis, S., Li, J.W., Ma, C.Q., Parada, M.A., Barra, F., Mittermayr, F., 2013. Pyrite as a record of hydrothermal fluid evolution in a porphyry copper system: a SIMS/EMPA trace element study. Geochim. Cosmochim. Acta 104, 42–62.

Reimold, W.U., Przybylowicz, W.J., Gibson, R.L., 2004. Quantitative major and trace elemental mapping by PIXE of concretionary pyrite from the Witwatersrand Basin, South Africa. X-ray spectrometry. Int. J. 33, 189–203.

Revan, M.K., Genç, Y., Maslennikov, V.V., Maslennikova, S.P., Large, R.R., Danyushevsky, L.V., 2014. Mineralogy and trace-element geochemistry of sulfide minerals in hy-drothermal chimneys from the Upper-Cretaceous VMS deposits of the eastern Pontide orogenic belt (NE Turkey). Ore Geol. Rev. 63, 129–149.

Rieger, A.A., Marschik, R., Díaz, M., Hölzl, S., Chiaradia, M., Akker, B., Spangenberg, J.E., 2010. The hypogene iron oxide copper-gold mineralization in the Mantoverde dis-trict, northern Chile. Econ. Geol. 105, 1271–1299.

Rusk, B., Oliver, N., Cleverley, J., Blenkinsop, T., Zhang, D., Williams, P., Habermann, P., 2010. Physical and chemical characteristics of the Ernest Henry iron oxide copper gold deposit, Australia; implications for IOGC genesis. In: Porter, T.M. (Ed.), Hydrothermal Iron Oxide Copper-Gold and Related Deposits: A Global Perspective. PGC Publishing, Adelaide, pp. 1–18.

Samama, J.C., Royer, J.J., N'Ganzi, C., 1989. Prise en compte de la surface spécifique des prélèvements en prospection géochimique: exemple de l'uranium dans les sédiments de ruisseau. J. Geochem. Explor. 32, 453–466.

Scott, R.J., Meffre, S., Woodhead, J., Gilbert, S.E., Berry, R.F., Emsbo, P., 2009. Development of framboidal pyrite during diagenesis, low-grade regional meta-morphism, and hydrothermal alteration. Econ. Geol. 104, 1143–1168.

Soltani Dehnavi, A., Lentz, D.R., McFarlane, C.R., 2015. LA-ICPMS analysis of volatile trace elements in massive sulphides and host rocks of selected VMS deposits of the Bathurst mining camp. New Brunswick: Methodology and application to exploration: In: Peter, J.M., Mercier-Langevin, P., (Eds.). Targeted Geoscience Initiative 4: Contributions to the understanding of volcanogenic massive sulphide deposit genesis and exploration methods development. Geol. Surv. Can. Open File 7853, pp. 59–80.

Soltani Dehnavi, A., McFarlane, C.R., Lentz, D.R., Walker, J.A., 2018. Assessment of pyrite composition by LA-ICP-MS techniques from massive sulfide deposits of the Bathurst Mining Camp, Canada: from textural and chemical evolution to its application as a vectoring tool for the exploration of VMS deposits. Ore Geol. Rev. 92, 656–671.

Sun, W.H., Zhou, M.F., Gao, J.F., Yang, Y.H., Zhao, X.F., Zhao, J.H., 2009. Detrital zircon U-Pb geochronological and Lu-Hf isotopic constraints on the Precambrian magmatic and crustal evolution of the western Yangtze Block, SW China. Precambr. Res. 172, 99–126.

Sung, Y.H., Brugger, J., Ciobanu, C.L., Pring, A., Skinner, W., Nugus, M., 2009. Invisible gold in arsenian pyrite and arsenopyrite from a multistage Archaean gold deposit: Sunrise Dam, Eastern Goldfields Province, Western Australia. Miner. Deposita 44, 765–791.

Tang, Y.Y., Bi, X.W., Zhou, J.X., Liang, F., Qi, Y.Q., Leng, C.B., Zhang, H., 2019. Rb-Sr isotopic age, S-Pb-Sr isotopic compositions and genesis of the ca. 200Ma Yunluheba Pb-Zn deposit in NW Guizhou Province, SW China. J. Asian Earth Sci. 185, 104054.

Thomas, H.V., Large, R.R., Bull, S.W., Maslennikov, V., Berry, R.F., Fraser, R., Froud, S., Moye, R., 2011. Pyrite and pyrrhotite textures and composition in sediments, laminated quartz veins, and reefs at Bendigo gold mine, Australia: insights for ore genesis. Econ. Geol. 106, 1–31.

Tribovillard, N., Algeo, T.J., Lyons, T., Riboulleau, A., 2006. Trace metals as paleoredox and paleoproductivity proxies: an update. Chem. Geol. 232, 12–32.

Ulrich, T., Long, D.G.F., Kamber, B.S., Whitehouse, M.J., 2011. In situ trace element and sulfur isotope analysis of pyrite in a paleoproterozoic gold placer deposit, Pardo and Clement Townships, Ontario, Canada. Econ. Geol. 106, 667–686.

Wang, C., Yang, L., Bagas, L., Evans, N.J., Chen, J., Du, B., 2018. Mineralization processes at the giant Jinding Zn-Pb deposit, Lanping Basin, Sanjiang Tethys orogen: evidence from in situ trace element analysis of pyrite and marcasite. Geol. J. 53, 1279–1294.

Wei, C., Huang, Z., Yan, Z., Hu, Y., Ye, L., 2018. Trace element contents in sphalerite from the Nayongzhi Zn-Pb deposit, Northwestern Guizhou, China: insights into incorporation mechanisms, metallogenic temperature and ore genesis. Minerals 8, 1–23.

Winderbaum, L., Ciobanu, C.L., Cook, N.J., Paul, M., Metcalfe, A., Gilbert, S., 2012. Multivariate analysis of an LA-ICP-MS trace element dataset for pyrite. Math. Geosci. 44, 823–842.

Woodhead, J.D., Hellstrom, J., Hergt, J.M., Greig, A., Maas, R., 2007. Isotopic and elemental imaging of geological materials by laser ablation inductively coupled plasma-mass spectrometry. Geostand. Geoanal. Res. 31, 331–343.

Xiao, C., Li, G.J., 2019. Geological, sulfur isotopic, and mineral trace element constraints on the genesis of the Xiyi Pb-Zn deposit, Baoshan Block, SW China. J. Asian Earth Sci. 186, 104056.

Xu, C., Zhong, H., Hu, R.Z., Wen, H.J., Zhu, W.G., Bai, Z.J., Fan, H.F., Li, F.F., Zhou, T., 2019. Sources and ore-forming fluid pathways of carbonate-hosted Pb-Zn deposits in Southwest China: implications of Pb-Zn-S-Cd isotopic compositions. Miner. Deposita 1–23.

Yan, D.P., Zhou, M.F., Song, H.L., Wang, X.W., Malpas, J., 2003. Origin and tectonic significance of a Mesozoic multi-layer over-thrust system within the Yangtze Block (South China). Tectonophysics 361, 239–254.

Ye, L., Cook, N.J., Ciobanu, C.L., Liu, Y., Zhang, Q., Liu, T., Gao, W., Yang, Y., Danyushevskiy, L., 2011. Trace and minor elements in sphalerite from base metal deposits in South China: a LA-ICPMS study. Ore Geol. Rev. 39, 188–217.

Yin, M.D., Huang, Z.L., Li, W.B., 2009. Rb-Sr isotopic dating of sphalerite from the giant Huize Pb-Zn ore field, Yunnan province, southwestern China. Chin. J. Geochem. 28, 70–75.

Zaw, K., Peters, S.G., Cromie, P., Burrett, C., Hou, Z., 2007. Nature, diversity of deposit types and metallogenic relations of South China. Ore Geol. Rev. 31, 3–47.

Zhang, Z.L., Huang, Z.L., Rao, B., Guan, T., Yan, Z.F., 2005. Concentration mechanism of ore-forming fluid in Huize lead-zinc deposits, Yunnan Province. Earth Sci. 30, 443–450.

Zhang, Z.B., Li, C.Y., Tu, G.C., Xia, B., Wei, Z.Q., 2006. Geotectonic evolution background and ore-forming process of Pb-Zn deposits in Chuan-Dian-Qian area of southwest China. Geotect. Metallo. 30, 343–354.

Zhang, C.Q., Yu, J.J., Mao, J.W., Rui, Z.Y., 2009. Advances in the study of Mississippi Valley-type deposits. Miner. Deposits 29, 195–210 (in Chinese with English abstract).

Zhang, J., Chen, Y.J., Pirajno, F., Deng, J., Chen, H.Y., Wang, C.M., 2013. Geology, C-H-O-S-Pb isotope systematics and geochronology of the Yindongpo gold deposit, Tongbai Mountains, central China: implication for ore genesis. Ore Geol. Rev. 53, 343–356.

Zhang, C.Q., Wu, Y., Hou, L., Mao, J.W., 2015. Geodynamic setting of mineralization of Mississippi Valley-type deposits in world-class Sichuan-Yunnan-Guizhou Zn-Pb triangle, Southwest China: implications from age-dating studies in the past decade and the Sm-Nd age of Jinshachang deposit. J. Asian Earth Sci. 103, 103–114.

Zhang, P., Huang, X.W., Cui, B., Wang, B.C., Yin, Y.F., Wang, J.R., 2016. Re-Os isotopic and trace element compositions of pyrite and origin of the Cretaceous Jinchang porphyry Cu-Au deposit, Heilongjiang Province, NE China. J. Asian Earth Sci. 129, 67–80.

Zhang, Y., Han, R., Wei, P., Wang, L., 2017. Identification of Two Types of Metallogenic Fluids in the Ultra-Large Huize Pb-Zn Deposit, SW China. Geofluids 1–22.

Zhao, H., Frimmel, H.E., Jiang, S., Dai, B., 2011. LA-ICP-MS trace element analysis of pyrite from the Xiaoqinling gold district, China: implications for ore genesis. Ore Geol. Rev. 43, 142–153.

Zheng, Y., Zhang, L., Chen, Y.J., Hollings, P., Chen, H.Y., 2013. Metamorphosed Pb-Zn-(Ag) ores of the Keketale VMS deposit, NW China: evidence from ore textures, fluid inclusions, geochronology and pyrite compositions. Ore Geol. Rev. 54, 167–180.

Zhou, C.X., Wei, C.S., Guo, J.Y., 2001. The source of metals in the Qilingchang Pb-Zn deposit, Northeastern Yunnan, China: Pb-Sr isotope constraints. Econ. Geol. 96, 583–598.

Zhou, M.F., Malpas, J., Song, X.Y., Kennedy, A.K., Robinson, P.T., Sun, M., Lesher, M., Keays, R.R., 2002. A temporal link between the Emeishan large igneous province (SW China) and the end-Guadalupian mass extinction. Earth Planet. Sci. Lett. 196, 113–122.

Zhou, J.X., Huang, Z.L., Yan, Z.F., 2013. The origin of the Maozu carbonate-hosted Pb-Zn deposit, southwest China: constrained by C-O-S-Pb isotopic compositions and Sm-Nd isotopic age. J. Asian Earth Sci. 73, 39–47.

Zhou, J.X., Xiang, Z.Z., Zhou, M.F., Feng, Y.X., Luo, K., Huang, Z.L., Wu, T., 2018. The giant Upper Yangtze Pb-Zn province in SW China: reviews, new advances and a new genetic model. J. Asian Earth Sci. 154, 280–315.

Zhu, C.W., Wen, H.J., Zhang, Y.X., Fan, H.F., 2016. Cadmium and sulfur isotopic compositions of the Tianbaoshan Zn-Pb-Cd deposit, Sichuan Province. China. Ore Geol. Rev. 76, 152–162.